JGR Atmospheres

RESEARCH ARTICLE
10.1029/2021JD036085

Special Section:
The land-air coupling over Tibetan Plateau and its global climate effects

Observational Constraint on the Contribution of Surface Albedo Feedback to the Amplified Tibetan Plateau Surface Warming

Yan Chen[1], Duoying Ji[1], John C. Moore[1,2,3], Jiangling Hu[1], and Yanyi He[4]

[1]College of Global Change and Earth System Science, Beijing Normal University, Beijing, China, [2]Arctic Centre, University of Lapland, Rovaniemi, Finland, [3]CAS Center for Excellence in Tibetan Plateau Earth Sciences, Beijing, China, [4]Department of Earth System Science, Ministry of Education Key Laboratory for Earth System Modeling, Institute for Global Change Studies, Tsinghua University, Beijing, China

Abstract Surface albedo feedback (SAF) is one of the main causes of amplified warming over the Tibetan Plateau (TP). Several recent studies have used the latest reanalysis datasets to evaluate the SAF induced warming, but without fully considering the fidelity of the surface albedo change and surface downward solar radiation in the reanalysis datasets, which directly affect the amplitude of SAF induced warming. This study finds that the state-of-the-art reanalysis datasets (ERA-Interim, ERA5, MERRA, MERRA-2, JRA-55 and CRA) and climate models that participated in the Coupled Model Intercomparison Project Phase 6 (CMIP6) exhibit varying biases compared with observations in both surface albedo change and surface downward solar radiation over the TP. The state-of-the-art reanalysis datasets present no obvious advantages over the lower resolution but less constrained CMIP6 multi-model ensemble in representing SAF related processes over the TP. The surface albedo change drives most of the spread in SAF induced warming. The reanalysis datasets and CMIP6 climate models reveal a significant linear relationship between surface albedo change and its contribution to surface temperature change over the TP. Using the observation constrained linear relationship and satellite surface albedo products, the spread of warming contribution due to SAF in reanalysis datasets and climate models is greatly reduced, the estimated TP warming due to SAF is in the range of 0.26–0.50 K in winter and 0.27–0.77 K in spring over recent decades.

Key Points:

- The Tibetan Plateau (TP) warming depends linearly on the strength of surface albedo feedback (SAF) in both reanalysis datasets and Coupled Model Intercomparison Project Phase 6 (CMIP6) models
- The spread of warming contribution due to SAF in reanalysis datasets and climate models over the TP is reduced by observational constraints
- Reanalysis datasets present no significant advantages over CMIP6 multi-model ensemble in representing SAF over the TP

Supporting Information:

Supporting Information may be found in the online version of this article.

Correspondence to:

D. Ji,
duoyingji@bnu.edu.cn

Citation:

Chen, Y., Ji, D., Moore, J. C., Hu, J., & He, Y. (2022). Observational constraint on the contribution of surface albedo feedback to the amplified Tibetan Plateau surface warming. *Journal of Geophysical Research: Atmospheres*, *127*, e2021JD036085. https://doi.org/10.1029/2021JD036085

Received 22 OCT 2021
Accepted 8 JUN 2022

1. Introduction

The Tibetan Plateau (TP) is warming faster than the rest of the Northern Hemisphere at the same latitudes (Liu & Chen, 2000), especially in winter. Even during the global warming hiatus in the first decade of the 21st century, a significant warming trend was measured over the TP (Duan & Xiao, 2015). The annual mean ground surface soil temperatures over the TP have warmed faster and more significantly than 2-m surface air temperatures during recent decades (Zhu et al., 2018). Many studies have addressed possible causes of rapid TP warming, such as changes in cloud amount and cloud-radiation feedback (Duan & Wu, 2006; Duan & Xiao, 2015; Pan et al., 2017), greenhouse effects caused by increases in water vapor (Rangwala et al., 2009; Rangwala & Miller, 2012), SAF due to snow cover change (Gao et al., 2019; Guo et al., 2018; Ji et al., 2020; Su et al., 2017), light-absorbing aerosol deposition on snowpack (Ji et al., 2015; Kang et al., 2019; Ma et al., 2019), and reduction of surface sensible heat flux and increases in heat storage (Wu et al., 2020). These mechanisms vary seasonally (Ji et al., 2020), and there is still no consensus on their relative importance (Kuang & Jiao, 2015; You et al., 2021).

Several recent studies (Gao et al., 2019; Ji et al., 2020; Su et al., 2017; Wu et al., 2020) used the perturbation surface energy budget equation (Lu & Cai, 2009b) and the coupled climate feedback-response analysis method (CFRAM, Lu & Cai, 2009a; Cai & Lu, 2009) to rank the relative importance of factors contributing to the amplified TP warming. Both methods are based on the surface energy budget equation, and are important tools for regional and global attribution studies as they can quantify the contribution of specific external forcing or climate processes to temperature change. Su et al. (2017), Gao et al. (2019) and Ji et al. (2020) applied the perturbation surface energy budget equation to the reanalysis datasets MERRA, MEERA-2 and JRA-55 finding that surface albedo feedback (SAF) and enhanced clear-sky downward longwave radiation heating are the dominant factors in the TP surface warming amplification, especially in winter. SAF warming works due to reductions in snowfall and increased snowmelt, leading to less snow cover over the TP and increased solar radiation absorption (Qu et al., 2019). Longwave radiative heating is the primary factor affecting the warming amplification in the Arctic,

while on TP it is SAF that most drives warming amplification in winter and spring (Gao et al., 2019). However, Wu et al. (2020) applied the CFRAM to the ERA-Interim reanalysis and found that changes in surface heat storage and surface sensible heat flux act to warm the surface temperature while changes in surface albedo tend to cool the surface of TP in winter. These opposing conclusions for the role of SAF in amplifying TP warming motivate us to carefully examine SAF effects diagnosed from the reanalysis datasets.

The contribution of SAF to surface temperature change depends on the surface albedo change and the surface downward shortwave radiation ($S^{\downarrow}$). Therefore, conclusions on the relative importance of various climate processes or external forcing rely on the quality of the reanalysis datasets. Atmospheric reanalysis datasets are created via a fixed assimilation-forecast model system which ingests available observations every several hours over the period being analyzed (Fujiwara et al., 2017). Observational constraints in reanalysis datasets vary considerably depending on the location, time period and variable considered. The scarcity of observational data over the TP might jeopardize the reliability of the reanalysis in the region. The surface albedo over the TP during winter and spring is greatly affected by the snow cover. Several state-of-the-art atmospheric reanalysis datasets produce hugely excessive snowpack over the TP (Orsolini et al., 2019) and exhibit very different interannual variations (Bian et al., 2020) from observed. It is speculated that excessive snowfall is the primary factor for the large overestimation of snow depth and cover in ERA5 reanalysis (Orsolini et al., 2019). Inappropriate snow cover parameterization (Jiang et al., 2019), especially the representation of shallow snow (Wang et al., 2020) in the land surface schemes used in reanalysis can also create spurious and excessive snow depth and snow cover, which then exert significant influences on surface albedo over the TP.

The $S^{\downarrow}$ in reanalysis datasets contains substantial biases (Wang et al., 2015) due to uncertainty in clouds and aerosols (Fujiwara et al., 2017), and drives variability in $S^{\downarrow}$ (e.g., Ghan et al., 2012; Wang et al., 2012). Observations of $S^{\downarrow}$ are sparse with limited spatiotemporal coverage (Wild, 2016), especially over the TP. Long-term variability in observed surface solar radiation and in reanalysis datasets shows significant $S^{\downarrow}$ biases (Feng and Wang., 2019; He et al., 2018; You et al., 2013; Zhang et al., 2020). For example, ERA-40 and NCEP/NCAR reanalysis datasets cannot capture the significant decreasing trend of all-sky surface solar radiation for the period 1960–2010 over the TP (You et al., 2013). Several widely used atmospheric reanalysis, such as CFSR, MERRA, MERRA-2, JRA-55 and ERA-Interim, all overestimate the multi-year mean solar radiation over China (Feng & Wang, 2019; Zhang et al., 2020). The biases in the $S^{\downarrow}$ are mostly attributed to cloud and aerosol simulation in the reanalysis systems. How these biases in surface albedo and $S^{\downarrow}$ in the reanalysis datasets might affect the estimated contribution of SAF to the TP warming has not yet been investigated.

Realistic surface albedo and surface downward shortwave radiation are the basis for understanding the surface energy budget and qualifying the contribution of SAF to regional temperature changes. Ground-based observations of $S^{\downarrow}$ and surface albedo are rare over the high elevation and cold environment of the TP. Atmospheric reanalysis datasets have a complete spatiotemporal coverage, but they suffer from various biases over high mountain regions (e.g., Li, et al., 2020; Orsolini et al., 2019; Yan et al., 2020). Previous generation climate models show largest spread in SAF over the TP (Qu & Hall, 2014). Therefore, a careful examination of the SAF as represented in reanalysis datasets and recent climate models compared with observations over the TP can lead to a better understanding of climate change over the TP. In this study, we use ground measurements of $S^{\downarrow}$, $S^{\downarrow}$ derived from sunshine duration data (SunDu-derived $S^{\downarrow}$), surface albedo data derived from satellite products, six state-of-the-art atmospheric reanalysis datasets and the most recent generation of climate models to study the contribution of SAF to the amplified TP warming in winter and spring seasons during the last several decades.

2. Data and Methods

2.1. In Situ Observations

Daily ground surface temperature (T_S) at 75 meteorological stations higher than 2000 m above sea level (a.s.l.) over the TP were retrieved from the China Meteorological Administration/China, 2012. Most of the stations are scattered in the central and eastern TP which cover more than half area of the TP, but only a few stations are located in the western TP (Figure 1).

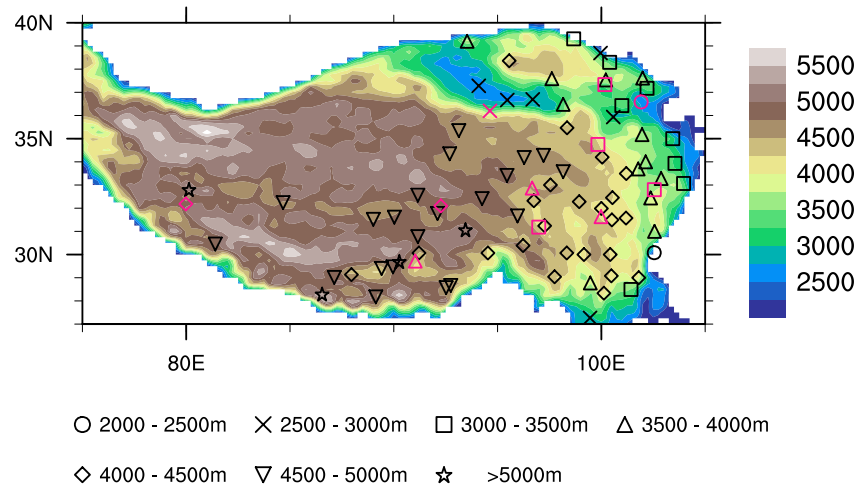

Figure 1. The spatial distribution of the meteorological stations used in this study, the elevation range of station is denoted by different markers, the terrain height (m) is denoted by the contour shading. The black markers represent the 75 meteorological stations providing ground measurements of surface temperature (T_S), the red markers represent the 11 stations providing ground measurements of surface downward shortwave radiation ($S^{\downarrow}$). SunDu-derived $S^{\downarrow}$ is available at all above stations, which are higher than 2000 m a.s.l.

2.2. Surface Downward Shortwave Radiation

Ground measurements of $S^{\downarrow}$ over the TP are sparse, so we use the $S^{\downarrow}$ data derived from meteorological observation of sunshine duration (SunDu-derived $S^{\downarrow}$, He et al., 2018) at the same 75 stations recording daily ground surface temperature. Existing studies have shown that the SunDu-derived $S^{\downarrow}$ can be used as a reliable proxy data for $S^{\downarrow}$ and it has better spatial-temporal coverage than ground measurements of $S^{\downarrow}$ (Feng & Wang, 2019; He et al., 2018; Manara et al., 2015). To further validate the SunDu-derived $S^{\downarrow}$ over the TP, we compare the SunDu-derived $S^{\downarrow}$ with ground measurements of $S^{\downarrow}$ at 11 stations higher than 2000 m a.s.l. over the TP (China Meteorological Administration/China, 2005).

2.3. Surface Albedo Data Sets

The CLARA-A2 (The CM SAF Cloud, Albedo And Surface Radiation data set from Advanced Very High Resolution Radiometer (AVHRR) data - Edition 2) data set provides surface albedo and surface radiation fields derived from the AVHRR satellite data. The data set covers a 34-year time period (1982–2015) at a spatial resolution of 0.25° × 0.25° (Karlsson et al., 2017). The retrieval algorithm in CLARA-A2 surface albedo included a mountainous topography correction and used a dynamic aerosol optical depth (AOD) time series for atmospheric correction. The CLARA-A2 data set and its earlier version (CLARA) have been used in the TP studies. For example, Guo et al. (2018) has evaluated the CLARA data set over the TP and found that it is suitable for quantifying long-term surface albedo changes and constraining the strength of SAF. Ma et al. (2019) has used the CLARA data set to study the role of SAF strengthened by black carbon in the enhanced warming over the Himalayas. Pang et al. (2022) has used the CLARA-A2 data set to quantify the relationships between the spatial and temporal patterns of the albedo and associated influencing factors over the TP. In this study, we use the monthly averages of black-sky surface albedo from CLARA-A2 data set.

The GLASS (Global LAnd Surface Satellites) surface albedo data set derived from AVHRR satellite data is based on a direct estimation algorithm using the surface reflectance, with radiometric calibration and atmospheric correction (Beijing Normal University, 2013; Liang et al., 2013). It provides a consistent albedo data set throughout the period of 1981–2018 with an accuracy that is comparable to that of the Moderate Resolution Imaging Spectroradiometer (MODIS) surface albedo product (He et al., 2013, 2014; Liu et al., 2013). The GLASS data set has been used to study the radiative cooling over the TP due to snow cover-induced surface albedo anomaly (Chen et al., 2017), and to evaluate surface albedo associated with optimizing snow cover parameterization schemes over the TP (Jiang et al., 2020). An et al. (2020) evaluated the performance of the GLASS satellite albedo product over the TP and found it coincides well with the ground-based observation. GLASS surface albedo is provided at

8-day intervals with a resolution of 0.05° × 0.05°. In this study we use its black-sky albedo and white-sky albedo of high quality (flags of 0 and 1) to calculate monthly mean blue-sky shortwave albedo, taking into account diffused skylight ratio in the shortwave range derived from the National Centers for Environmental Prediction (NCEP) reanalysis as described in He et al. (2014). For the GLASS data set averaged over the entire TP during winter and spring, the difference between climatological black-sky albedo and blue-sky albedo is in the range of 0.0008–0.0058, and the difference between changes in black-sky albedo and blue-sky albedo over the two climate periods is in the range of 0.0003–0.0006. The rather small difference between black-sky albedo and blue-sky surface albedo has been reported in previous studies (e.g., Liu et al., 2009; Manninen et al., 2012) and this holds true for the GLASS data set over the TP as well. Therefore, in this study the CLARA-A2 black-sky albedo and GLASS blue-sky albedo are compared directly with the surface albedo derived from the reanalysis datasets and climate models.

The CLARA-A2 and GLASS surface albedo datasets are both derived from AVHRR satellite data but using different retrieval algorithms and of different spatio-temporal resolutions. Since all observation-based products relating to snow and albedo contain significant uncertainties (Brown & Derksen, 2013), we treat the difference between CLARA-A2 and GLASS as observational uncertainty in surface albedo for both climatology and long-term change.

2.4. Reanalysis Data Sets

We use six sets of "full-input" reanalysis datasets, which assimilate both conventional and satellite data from the surface and upper-air (Fujiwara et al., 2017). ERA-Interim (Dee et al., 2011) was initially released in 2008 by European Centre for Medium-Range Weather Forecasts, 2012. ERA-Interim has a horizontal resolution of 0.75° × 0.75° and temporal resolution of 6 hr and it is widely used in climate change studies for the TP. ERA5 (Hersbach et al., 2019) was recently released by European Centre for Medium-Range Weather Forecasts (2019) to supersede ERA-Interim. ERA5 improves on ERA-Interim with a horizontal resolution of 0.25° × 0.25° and temporal resolution of 1 hr. MERRA (Rienecker et al., 2011) was released in 2009 by NASA's Global Modeling and Assimilation Office, 2008, it has a horizontal resolution of 0.5° × 0.667° and temporal resolution of 1 hr. MERRA-2 (Bosilovich et al., 2015), a follow-up product to MERRA, was released in 2015 by NASA's Global Modeling and Assimilation Office (2015) with a horizontal resolution of 0.5° × 0.625° and temporal resolution the same as MERRA. JRA-55 (Kobayashi et al., 2015) was released by the Japan Meteorological Agency 2013 with a horizontal resolution of 0.562° × 0.562° and temporal resolution of 6 hr. CRA was released in 2021 from CMA as its first-generation 40-year global atmosphere and land reanalysis product and extends to 1979. CRA assimilates more Chinese observed surface and radiosonde data than other reanalysis products and uses more than 50 kinds of satellite observations (China Meteorological Administration/China, 2021; Wang et al., 2018). The monthly CRA data set with a horizontal resolution of 0.31° × 0.31° was used in this study. The ERA5, MERRA-2, JRA-55 and CRA belong to the latest generation of atmospheric reanalysis data set.

The six reanalysis datasets used in this study do not assimilate any $S^{\downarrow}$ from conventional or satellite observations. $S^{\downarrow}$ derived from these reanalysis datasets is calculated using radiation transfer models. The six reanalysis datasets also do not assimilate any surface albedo data, but some of them do use some surface albedo parameters from satellite data, for example, MERRA and MERRA-2 used MODIS climatological surface albedo parameters (Reichle et al., 2017). JRA-55 calculates the land surface albedos by solving the equation of radiative transfer in vegetation canopies without assimilating satellite data (Kobayashi et al., 2015). The six reanalysis datasets assimilate snow depth and snow cover to various extents, and usually snow cover fraction is derived empirically from snow depth (Orsolini et al., 2019). ERA-Interim assimilates the Interactive Multisensor Snow and Ice Mapping System (IMS) snow cover at high altitudes, while ERA5 only assimilates IMS snow cover at altitudes below 1500 m a.s.l. Neither ERA-Interim nor ERA5 assimilates in situ observational snow information. JRA-55 assimilates snow depth from a dozen CMA stations over the TP and snow cover from satellite data. MERRA and MERRA-2 do not assimilate any observational snow information, but MERRA-2 uses observed precipitation data, and has a better performance than MERRA in terms of snow cover and snow depth (Orsolini et al., 2019). We derive land surface albedo of the six reanalysis datasets by calculating the ratio between upward shortwave radiation and downward shortwave radiation at the surface, the upward shortwave radiation is obtained by subtracting net solar radiation from downward shortwave radiation.

2.5. CMIP6 Models

Climate models show that TP is one of the most important regions determining northern hemisphere SAF, and the largest spread in SAF occurs over TP (Qu & Hall, 2014). We collected the Atmospheric Model Intercomparison Project (AMIP) simulations from 28 climate models (Table S1 in Supporting Information S1) that participated in the CMIP6 (Eyring et al., 2016) to diagnose the surface albedo change and its contribution to TP warming during the recent decades. The AMIP simulation was driven by observational sea surface temperature and sea ice concentration and hence the models were expected to produce realistic historical global warming. To ensure an equal weight for different climate models, we selected the first ensemble AMIP run (r1i1p1f1) from the 28 CMIP6 models. The CMIP6 models have horizontal resolutions varying from 2.815° × 2.815° to 0.703° × 0.703°, with most resolutions lower than 1° × 1°, which is much coarser than the reanalysis datasets. Most AMIP simulations cover 1979–2014, and we select the period of 1982–2014 to align with the time window of the observations used in this study.

2.6. Methods

The perturbation surface energy budget equation (Lu & Cai, 2009b) is used to calculate the contributions of the dynamic and thermal processes to the surface temperature change. The relative importance of climate processes and external forcing to the TP ground surface temperature change over the two climate periods 1982–1998 and 1999–2014 are compared. Observations and reanalysis datasets extend to 2015 so the second period is 1 year longer in their case. Following Lu and Cai (2009b), the surface energy budget equation and its perturbation form can be written as Equations 1 and 2 respectively:

$$\mathrm{Q} = (1-\alpha)S^{\downarrow} + F^{\downarrow} - F^{\uparrow} - H - LE \tag{1}$$

$$4\sigma\overline{T}_s^3\Delta T_s \approx -\Delta\alpha\left(\overline{S^{\downarrow}} + \Delta S^{\downarrow}\right) + \Delta\mathrm{CRF_s} + \left(1-\overline{\alpha}\right)\Delta S^{\downarrow\mathrm{clr}} + \Delta F^{\downarrow\mathrm{clr}} - \Delta Q - \Delta(H+\mathrm{LE}) \tag{2}$$

where α is surface albedo, $S^{\downarrow}$ is surface downward shortwave radiation, $F^{\downarrow}$ is surface downward longwave radiation, $F^{\uparrow}$ is surface upward longwave radiation with $F^{\uparrow} \approx \sigma T_s^4$ assuming the surface emissivity to be one at all wavelengths, H and LE are surface sensible and latent heat fluxes. Q is land surface heat storage, by applying Equation 1 in both the first and second climate periods, the heat storage change term (ΔQ) can be obtained from their difference (Lu & Cai, 2009b). The overbar ($\bar{}$) in Equation 2 denotes the average climate state in the first period 1982–1998, Δ denotes the difference between the second and first climate periods, and $(\cdot)^{\mathrm{clr}}$ denotes the clear sky state, $\sigma = 5.67\times10^{-8}\,W\cdot m^{-2}\cdot K^{-4}$ is the Stefan-Boltzmann constant, and $\mathrm{T_S}$ is ground surface temperature. Equation 2 decomposes the change of ground surface temperature ($\Delta\mathrm{T_S}$) to six contributing terms representing dynamical and thermodynamic climate processes. The terms on the right-hand side of Equation 2 respectively represent SAF ($-\Delta\alpha\left(\overline{S^{\downarrow}} + \Delta S^{\downarrow}\right)$), change of cloud radiative forcing (ΔCRFs), change of clear-sky downward shortwave radiation ($\left(1-\overline{\alpha}\right)\Delta S^{\downarrow\mathrm{clr}}$), change of clear sky downward longwave radiation ($\Delta F^{\downarrow\mathrm{clr}}$), change of ground heat storage (ΔQ) and change of surface turbulent heat exchanging with the atmosphere ($\Delta(H+\mathrm{LE})$). According to Lu and Cai (2009b), ΔCRFs is defined as the difference between the change of net total-sky radiation and the change of net clear-sky radiation at the surface, which excludes the SAF by only retaining the mean surface albedo term, and equals to $\left(1-\overline{\alpha}\right)\Delta S^{\downarrow,\mathrm{cld}} + \Delta F^{\downarrow,\mathrm{cld}}$, where $(\cdot)^{\mathrm{cld}}$ denotes difference between total-sky condition and clear-sky condition. By multiplying the sensitivity parameter $\left(1/\left(4\sigma\overline{T_S}^3\right)\right)$ with the six contributing terms in the right-land side of Equation 2, we get the partial temperature changes (PTCs) due to six climate processes denoted as $\Delta\mathrm{T_{SAF}}$, $\Delta\mathrm{T_{CRF}}$, $\Delta\mathrm{T_{SW}}$, $\Delta\mathrm{T_{LW}}$, $-\Delta\mathrm{T_Q}$ and $-\Delta\mathrm{T_{H+LE}}$ respectively. Specifically, the contribution of SAF to surface temperature change is:

$$\Delta\mathrm{T}_{SAF} = \frac{-\Delta\alpha\left(\overline{S^{\downarrow}} + \Delta S^{\downarrow}\right)}{4\sigma\overline{T}_s^3} \tag{3}$$

Fields involved in Equation 2 can be obtained or calculated from ERA5, MERRA, MERRA-2, JRA-55, CRA reanalysis datasets and CMIP6 climate models. In the case of ERA-Interim which lacks clear-sky fields we

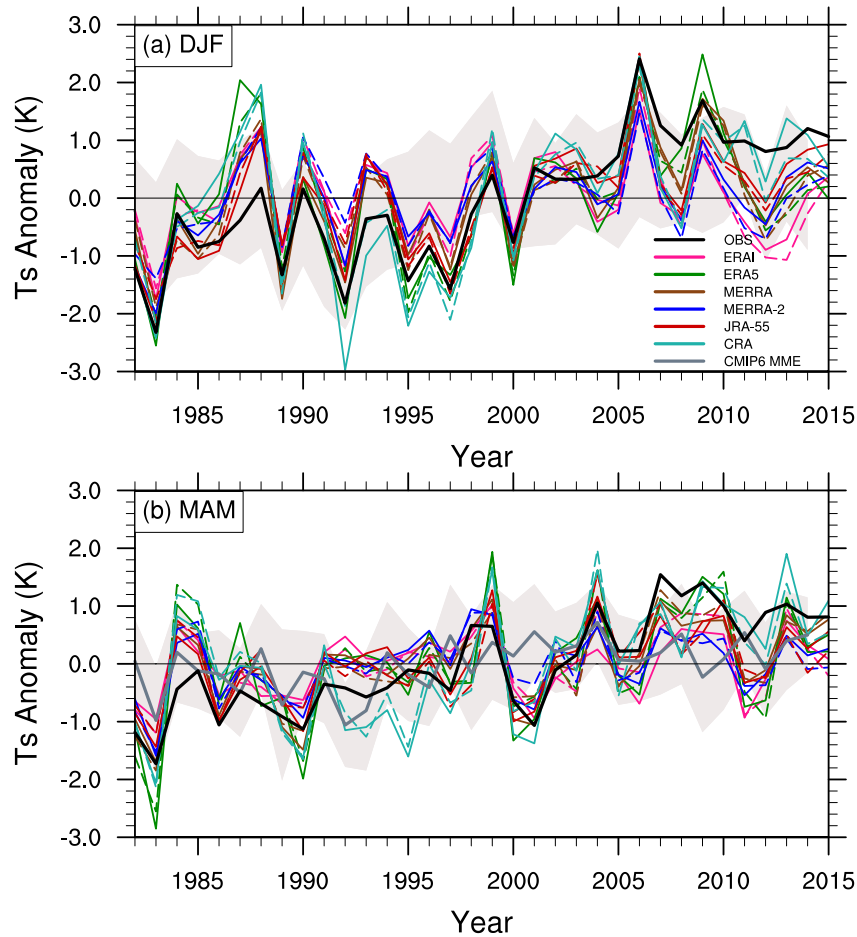

Figure 2. Winter (DJF, a) and spring (MAM, b) mean surface temperature (T_S) anomalies over the 75 meteorological stations (solid lines) and the entire TP (dash lines) above 2000 m a.s.l. during 1982–2015. The black curve is the result of the 75 stations averaged observation, and the pink, green, brown, blue, red, seagreen and darkgray lines represent ERA-Interim (ERAI), ERA5, MERRA, MERRA-2, JRA-55, CRA and Coupled Model Intercomparison Project Phase 6 (CMIP6) multi-model ensemble (CMIP6 MME) mean, respectively. The light gray shading denotes the one standard derivation of the CMIP6 models below/above the CMIP6 MME mean.

only calculate the PTCs due to SAF (ΔT_{SAF}), surface heat storage ($-\Delta T_Q$) and surface turbulent heat fluxes ($-\Delta T_{H+LE}$). All calculations use monthly mean values. For calculations over the observation stations, the satellite datasets, reanalysis datasets and CMIP6 models are bilinearly interpolated to the locations of observation stations. For calculations over the entire TP, we use the raw resolution of each data set and select grid cells of satellite datasets, reanalysis datasets and CMIP6 models enclosed in the TP region higher than 2000 m a.s.l. without applying spatial interpolation.

3. Results

3.1. Surface Temperature Changes

The observed T_S change between the two climate periods 1982–1998 and 1999–2015 averaged over the 75 stations is 1.66 ± 0.78 K for winter (DJF) and 1.12 ± 0.61 K for spring (MAM). T_S is relatively flat during 1982–1998 but increases significantly during 1999–2015 (Figure 2). The six reanalysis datasets and CMIP6 models can reproduce much of the decadal temperature variation shown in the 75-station averaged observations. Only CRA of the reanalysis datasets can reproduce realistic winter (1.39 ± 1.17 K) and spring (1.21 ± 0.86 K) warmings, with the other five reanalysis datasets underestimating both winter and spring warmings. ERA-Interim shows least warming (0.22 ± 0.77 K for winter and 0.08 ± 0.54 K for spring). The underestimated TP warming in

reanalysis datasets has been noted in previous studies (e.g., Yan et al., 2020). The CMIP6 multi-model ensemble (CMIP6 MME) mean warming between the two climate periods is 0.67 ± 0.46 K for winter and 0.52 ± 0.23 K for spring, and the majority of CMIP6 models underestimate the observed warming. Only CESM2, CESM2-FV2 and NorCPM1 produce more than 80% of the 75-station averaged warming for winter and CESM2 and FGOALS-f3-L for spring. Most reanalysis datasets and CMIP6 models only realized about half of the observed warming amplitude, but the six reanalysis datasets and CMIP6 MME mean show larger winter warming than spring warming, which is consistent with the observations.

The decadal variations and warming trends from both the reanalysis datasets and CMIP6 models over the entire TP at elevations above 2000 m a.s.l. are similar to the 75-station averaged results (Figure 2), which indicates that the 75 stations can represent the entire TP in terms of amplified warming between the two climate periods, despite most stations being in the central and eastern TP. The discrepancies in surface temperature change among the reanalysis datasets, climate models and observations might be attributed to deficiencies in the physical parameterization schemes, not enough observations assimilated in the reanalysis system, and inaccurate topography used in climate models and reanalysis systems and their differences from the locations of meteorological stations (Yan et al., 2020).

3.2. Surface Albedo

The contribution of SAF to the TP warming depends on the surface albedo change, surface downward shortwave radiation and its change over time. Among these factors, the surface albedo change usually determines the magnitude of SAF (Colman, 2013; Li et al., 2016; Loranty et al., 2014). Satellite data shows that on average 16% of the entire TP is covered by snow with more snow in winter (Basang et al., 2017). Several state-of-the-art reanalysis datasets have significant biases in snow depth and snow cover over the TP (Orsolini et al., 2019), these biases can result in unrealistic surface albedo over the TP and affect the surface energy budgets. In the following, we use the CLARA-A2 and GLASS surface albedo datasets to evaluate the performance of reanalysis datasets and CMIP6 models over the TP in terms of climatology and changes over the two climate periods.

Figure 3a shows the climatological surface albedo averaged over the 75 stations and the entire TP above 2000 m a.s.l. in winter (DJF) and spring (MAM). The 75-station averaged surface albedo is 0.21 ± 0.08 and 0.21 ± 0.07 in winter, 0.21 ± 0.07 and 0.20 ± 0.07 in spring for CLARA-A2 and GLASS respectively. The entire TP averaged surface albedo is 0.24 in winter for both satellite products, 0.25 and 0.24 in spring for CLARA-A2 and GLASS respectively. As both surface albedo products are derived from AVHRR satellite data, it is expected that they share nearly same seasonal climatology. For the surface albedo climatology over the 34-year period from 1982 to 2015, only MERRA and MERRA-2 are close to the satellite products, the other four reanalysis datasets, especially for ERA5, JRA-55 and CRA overestimate surface albedo in both winter and spring. MERRA-2 shows the best performance in surface albedo climatology and this might be due to its usage of observed precipitation data improving snow depth and snow cover simulation (Orsolini et al., 2019). The spread of surface albedo climatology among the six reanalysis datasets is large, comparable to the magnitude of surface albedo represented by the satellite products. The majority of CMIP6 models have larger surface albedo than the satellite products, but a few are close to or even smaller than the satellite products. The CMIP6 MME mean surface albedo over the entire TP is 0.42 ± 0.09 in winter and 0.34 ± 0.08 in spring. The serious surface albedo biases in winter and spring are probably due to excessive snowfall and cold temperature biases over the TP, implying deficiencies in the representation of snow-ice albedo in the climate models (Gao et al., 2015; Su et al., 2013; Yan et al., 2020). Systematic overestimation of surface albedo may result in cold temperature bias in the Northern Hemisphere, especially at high altitudes (Li et al., 2016). The overestimated surface albedo and cold biases over the TP in the reanalysis datasets and climate models likely interact with each other through snow albedo feedback.

Figure 3b shows that the surface albedo has decreased over the two climate periods, and GLASS generally exhibits larger surface albedo reduction than does CLARA-A2. The range of surface albedo change ($\Delta\alpha$) averaged over the 75 stations is −0.004 to −0.012 for winter, and −0.005 to −0.010 for spring (Table S2 in Supporting Information S1) with similar ranges for the entire TP above 2000 m a.s.l (Table S3 in Supporting Information S1). The satellite surface albedo averaged over the entire TP decreases by 2.0%–4.5% in winter and by 2.0%–5.8% in spring over two climate periods, depending on the product. These are close to the decreasing trends in surface albedo over the Arctic since the 1980s (Zhang et al., 2019). Although CLARA-A2 and GLASS are both derived from AVHRR satellite data and have nearly same surface albedo climatology over the TP, there is a relatively

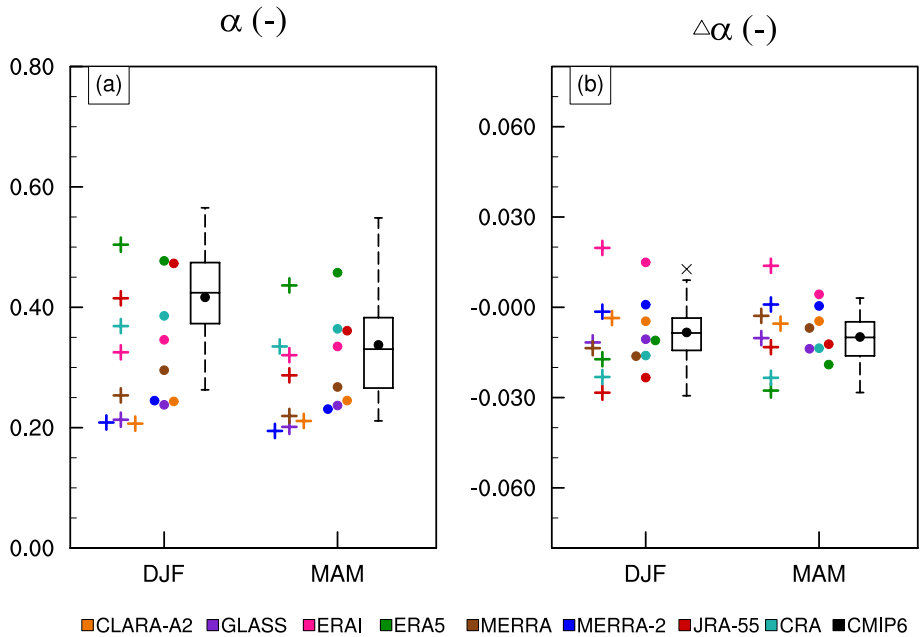

Figure 3. Surface albedo climatology over the whole study period (a) and surface albedo change over two climate periods (b) for winter (DJF) and spring (MAM). Colored cross markers denote satellite products and reanalysis datasets averaged over the 75 meteorological stations. Colored solid dot markers denote satellite products and reanalysis datasets averaged over the entire Tibetan Plateau (TP) above 2000 m a.s.l. Boxplots denote Coupled Model Intercomparison Project Phase 6 (CMIP6) models averaged over the entire TP above 2000 m a.s.l, with each box represents the 25th and 75th percentiles (the interquartile range), the horizontal line in box represents the median, the ends of the whiskers represent the range of values falling within 1.5 inter-quartiles from the median. Solid dot in boxplot represents CMIP6 multi-model ensemble mean averaged over the entire TP.

large discrepancy in their changes over two climate periods. The spread of surface albedo change can be attributed to difficulties in distinguishing snow cover and cloud, especially the distinct characteristics of snow cover over the TP, which are often shallow, patchy and frequently of short duration (Qin et al., 2006). As stated earlier, the range of surface albedo changes from two satellite albedo products is taken as observational uncertainty and is used to estimate uncertainty in snow albedo feedback over the TP.

The reanalysis datasets exhibit a much larger spread in the TP averaged surface albedo change than the two satellite products (Figure 3 and Table S3 in Supporting Information S1). MERRA, CRA and JRA-55 overestimate the surface albedo reduction in winter compared with the two satellite products, ERA5 overestimates surface albedo reduction in spring. Only ERA5 has its winter surface albedo reduction in the observational range −0.005 to −0.011, MERRA, JRA-55 and CRA have their spring surface albedo reduction in the observational range −0.005 to −0.014 given by the two satellite products. MERRA-2 exhibits very weak surface albedo change in both winter and spring, although it has best performance in seasonal climatology of surface albedo. ERA-Interim shows an opposite trend in surface albedo change from the satellite products and other reanalysis datasets in both winter and spring. Increasing surface albedo over the TP in ERA-Interim was previously reported by Wu et al. (2020). For the CMIP6 models, the multi-model ensemble mean surface albedo change averaged over the entire TP is -0.008 ± 0.010 for winter and -0.010 ± 0.008 for spring, both of them are within the range given by the two satellite products. The spread of surface albedo change in CMIP6 models is comparable to that of the six reanalysis datasets (Figure 3b). Hence, the six analysis datasets do not show obvious advantages over the CMIP6 models in representing TP surface albedo change, although the reanalysis datasets have assimilated various kind of observations.

Figure 4 shows the spatial distributions of surface albedo change for mean results of satellite datasets, reanalysis datasets (excluding ERA-Interim) and CMIP6 models. Figure S1 Supporting Information S1 shows the spatial distributions of surface albedo change for individual reanalysis datasets. The reanalysis datasets can reproduce the notable surface albedo increase at the northern TP in winter (Figures 4a and 4c) and decrease at the southwestern

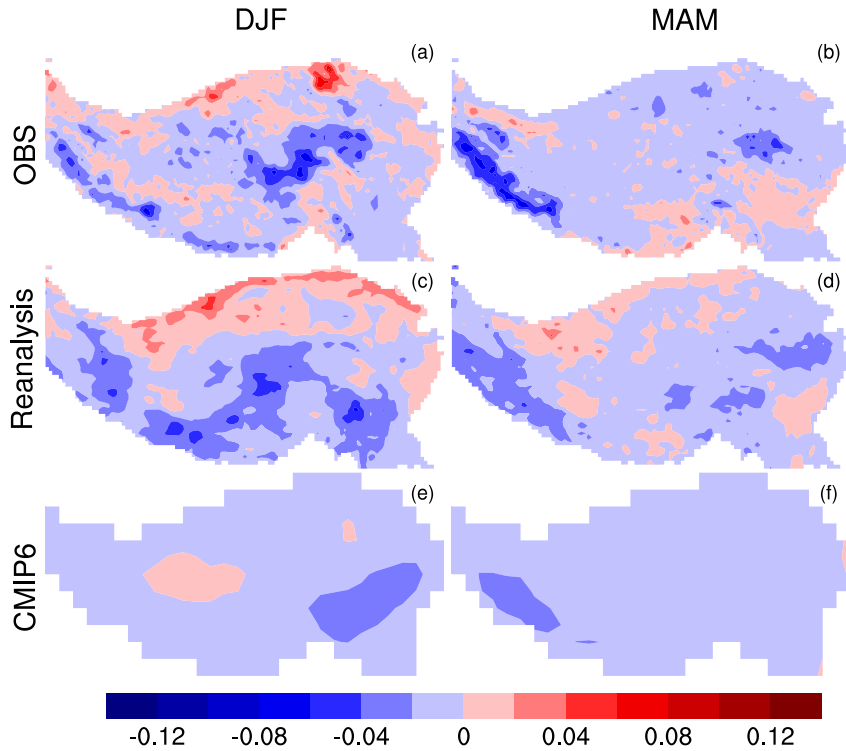

Figure 4. The spatial distributions of surface albedo change ($\Delta\alpha$) from 1982 to 1998 to 1999–2015 in winter (DJF, left column) and spring (MAM, right column) for mean results of two satellite surface albedo datasets (CLARA-A2 and GLASS) (a and b), five reanalysis datasets (ERA5, MERRA, MERRA-2, JRA-55 and CRA) (c and d) and Coupled Model Intercomparison Project Phase 6 (CMIP6) multi-model ensemble mean (e and f) over the entire Tibetan Plateau.

TP in spring (Figures 4b and 4d). The reanalysis can also reproduce the general surface decrease in the central TP in winter and spring. Contrary to satellite datasets and other reanalysis datasets, ERA-Interim presents relatively large surface albedo increases over the central and eastern TP (27°N ~ 40°N, 82°E ~105°E, the black box as shown in Figures S1a and S1b in Supporting Information S1), which causes the entire TP averaged surface albedo to increase over the two climate periods (Figure 3b). This might be ascribed to its assimilation of gridded snow cover data from IMS since 2004 (Orsolini et al., 2019), as ERA-Interim shows an abrupt increase in surface albedo and larger inter-annual snow cover variations over the middle and eastern TP since 2004 (Figure S2 in Supporting Information S1). The CMIP6 MME mean cannot reproduce the notable surface albedo changes on the northern TP in winter (Figure 4e), but can reproduce the decrease at the southwestern TP with a smaller spatial extent in spring (Figure 4f). The relatively uniform decrease in surface albedo represented in the CMIP6 models might be attributed to their coarse horizontal resolution without adequate description of the complex terrain over the TP. In addition, there is large inter-model variation in the spatial distribution of surface albedo change over the TP for the CMIP6 models (not shown), and CMIP6 MME mean surface albedo change more likely reflects the response of surface albedo to external climate forcing and topography varying across the TP.

3.3. Surface Downward Shortwave Radiation

Previous studies have found that several widely used atmospheric reanalysis datasets overestimate the multi-year mean $S^{\downarrow}$ over China and have larger relative biases in winter and spring than in other seasons (Feng & Wang, 2019; Zhang et al., 2020). SunDu-derived $S^{\downarrow}$ has a good agreement with ground measurements of $S^{\downarrow}$ and better spatial-temporal coverage compared with ground measurements (He et al., 2018; Wang et al., 2015). Figure 5 compares $S^{\downarrow}$ from SunDu-derived data set, reanalysis datasets and CMIP6 climate models with the ground measurements at 11 stations over the TP. The anomalously low values before 1993 in the ground measurements of $S^{\downarrow}$ is mainly due to instrument change (Tang et al., 2011; Wang et al., 2015) and excluded in the following analysis. The significant decadal declining trend since 1994 in the ground measurements of $S^{\downarrow}$ has been

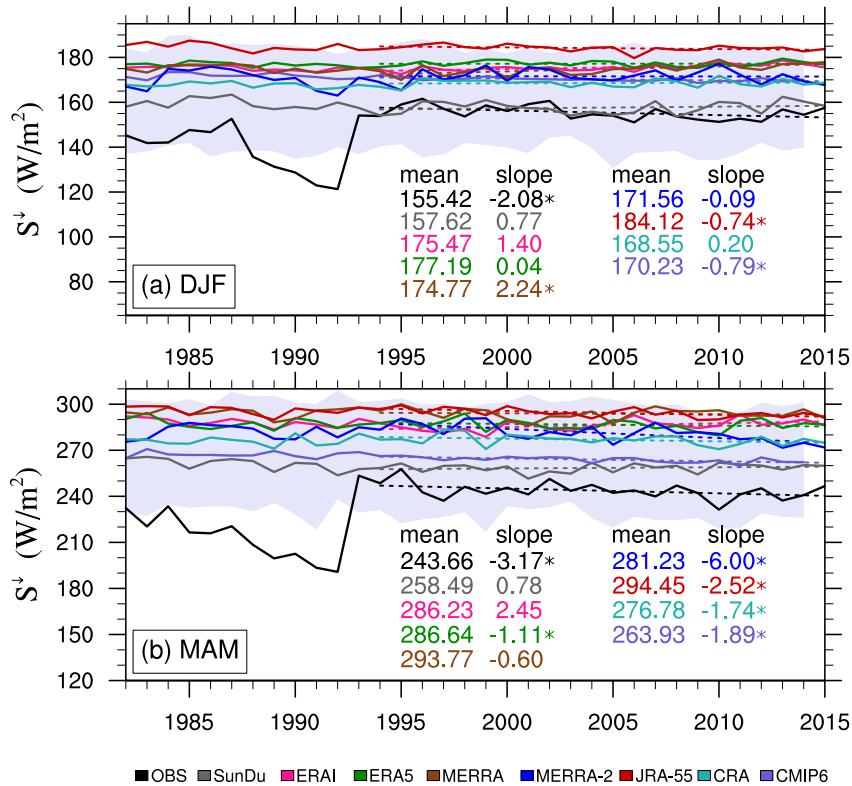

Figure 5. Comparison of surface downward shortwave radiation ($S^{\downarrow}$) from ERA-Interim (ERAI), ERA5, MERRA, MERRA-2, JRA-55, CRA and Coupled Model Intercomparison Project Phase 6 (CMIP6) multi-model ensemble (MME), SunDu-derived data set and observations averaged at the 11 ground measurement stations over the Tibetan Plateau for winter (DJF, a) and spring (MAM, b). The linear regression (dashed lines) and time mean are calculated over the period of 1994–2015 (1994–2014 for the CMIP6 models). The mean (units of W/m^2) and linear trend (slope, units of W/m^2/10 years) are labeled for each data set. The * marker indicates a linear regression is significant at the 95% confidence level with $p \leq 0.05$. The light shading denotes the one standard derivation of the CMIP6 below/above the CMIP6 MME mean.

explained as mainly due to the increase in water vapor and deep cloud cover related to rapid TP warming (Yang et al., 2012). The SunDu-derived $S^{\downarrow}$ well represents ground measurements of $S^{\downarrow}$ in terms of multi-year seasonal mean, especially in winter (Figure 5a). In spring, the SunDu-derived data overestimates $S^{\downarrow}$ by about 14.8 W/m^2. In contrast, the reanalysis datasets overestimate the seasonal mean of $S^{\downarrow}$, by between 13.1 W/m^2 and 28.7 W/m^2 in winter and between 33.1 W/m^2 and 50.8 W/m^2 in spring. Among the six reanalysis datasets, CRA presents smallest $S^{\downarrow}$ biases in both winter and spring, while JRA-55 presents the largest $S^{\downarrow}$ biases in both winter and spring. The CMIP6 MME mean $S^{\downarrow}$ is generally closer to both the ground measurements of $S^{\downarrow}$ and SunDu-derived $S^{\downarrow}$ than are the reanalysis datasets, especially in spring. The $S^{\downarrow}$ discrepancies between the SunDu-derived data set and ground measurements are substantial less than the biases of the reanalysis datasets and CMIP6 climate models relative to the ground measurements.

Figure 6 compares $S^{\downarrow}$ of the reanalysis datasets with SunDu-derived $S^{\downarrow}$ at the same 75 stations selected for comparing surface albedo and surface temperature. The six reanalysis datasets overestimate the 75-station averaged $S^{\downarrow}$ by between 9.9 W/m^2 and 28.7 W/m^2 in winter, and by between 16.1 W/m^2 and 41.9 W/m^2 in spring (Figure 6a and Table S2 in Supporting Information S1). While SunDu-derived $S^{\downarrow}$ does not reproduce the declining trend at the 11 $S^{\downarrow}$ ground measurement stations from 1994 to 2014 (Figure 5), it does show an obvious decline at the 75 meteorological stations, by −0.33 W/m^2 in winter and −1.82 W/m^2 for spring between the two climate periods (Figure 6b and Table S2 in Supporting Information S1). The declining trend of SunDu-derived $S^{\downarrow}$ seen as more stations are used increases its credibility for the TP as a whole. All reanalysis datasets show a $S^{\downarrow}$ decline in spring, but only JRA-55 can reproduce the declining trend of $S^{\downarrow}$ in winter. JRA-55 exhibits a realistic $S^{\downarrow}$ declining trend compared with the ground measurements at the 11 stations (Figure 5) and SunDu-derived $S^{\downarrow}$ at the 75 meteorological stations (Figure 6b), although JRA-55 has one of the largest $S^{\downarrow}$ biases in seasonal mean.

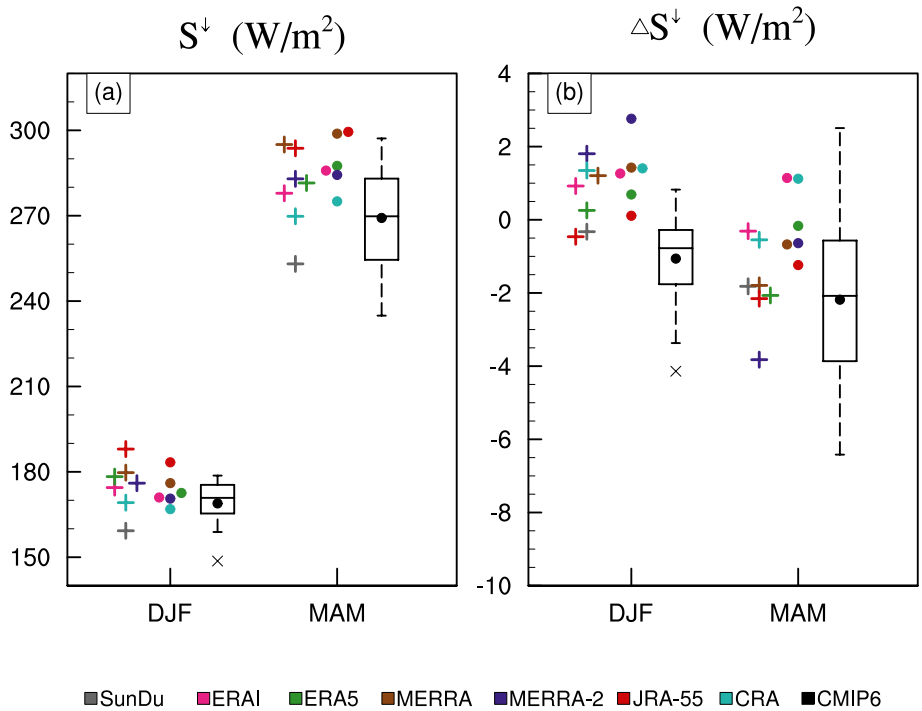

Figure 6. Surface downward shortwave radiation ($S^{\downarrow}$) climatology over the whole study period (a) and change over two climate periods (b) for winter (DJF) and spring (MAM). Colored cross markers denote SunDu-derived and reanalysis datasets averaged over the 75 stations. Colored solid dot markers denote SunDu-derived $S^{\downarrow}$ and reanalysis datasets averaged over the entire Tibetan Plateau (TP) above 2000 m a.s.l. Boxplot denotes Coupled Model Intercomparison Project Phase 6 (CMIP6) models averaged over the entire TP above 2000 m a.s.l, with each box represents the 25th and 75th percentiles (the interquartile range), the horizontal line in box represents the median, the ends of the whiskers represent the range of values falling within 1.5 inter-quartiles from the median. Solid dot in boxplot represents CMIP6 multi-model ensemble mean value averaged over the entire TP.

Figure 6 also compares the TP averaged $S^{\downarrow}$ for the six reanalysis datasets and CMIP6 climate models. Generally, the reanalysis datasets present larger $S^{\downarrow}$ than CMIP6 MME mean $S^{\downarrow}$, except for CRA in winter. On the other hand, CMIP6 models present a relatively larger spread in $S^{\downarrow}$ than do the six reanalysis datasets. For the entire TP averaged $S^{\downarrow}$ changes over the two climate periods, CMIP6 MME mean shows an $S^{\downarrow}$ decrease in winter, while the six reanalysis datasets all suggest $S^{\downarrow}$ increases. In spring, ERA-Interim and CRA suggest $S^{\downarrow}$ increases, while the other four reanalysis datasets and CMIP6 MME mean suggest $S^{\downarrow}$ decreases. In both seasons, the CMIP6 MME mean changes in $S^{\downarrow}$ are closer to the 75 station-averaged SunDu-derived $S^{\downarrow}$ changes than that of most reanalysis datasets. The poor performance of the reanalysis and climate models on representing the mean and declining trend of $S^{\downarrow}$ is likely due to the atmospheric factors, such as cloud coverage and water vapor content (Zhang et al., 2020) or the neglect of time varying aerosol in reanalysis assimilation systems (You et al., 2013). The inability of reanalysis datasets and climate models to correctly reproducing the decline in $S^{\downarrow}$ exerts only minor impacts on the mean $S^{\downarrow}$ (Table S2 and S3 in Supporting Information S1). Therefore, in Equation 3 the magnitude of $\overline{S^{\downarrow}} + \Delta S^{\downarrow}$ is overwhelmingly determined by $\overline{S^{\downarrow}}$.

Figure 7 shows the spatial distributions of $\Delta S^{\downarrow}$ derived from SunDu-derived $S^{\downarrow}$ at the 75 stations and the mean results from the reanalysis datasets (excluding ERA-Interim) and CMIP6 models over the entire TP. In winter, the reanalysis datasets can reproduce the increasing $S^{\downarrow}$ over the southern TP as shown in the SunDu-derived $\Delta S^{\downarrow}$ (Figures 7a and 7c). In spring, the reanalysis datasets can capture the spatial pattern of SunDu-derived $\Delta S^{\downarrow}$ with increases mostly over the northern TP and decreases over the central and southeastern TP (Figures 7b and 7d). The spatial pattern of $\Delta S^{\downarrow}$ mainly reflects changes in cloud amounts. Most of station observations across the central and eastern TP show decreasing trends in total cloud cover and the most significant decrease occurs in the central TP (Duan & Wu, 2006; You et al., 2014). Satellite and reanalysis dataset. also highlight long-term decreasing trends of cloud cover over TP during cold seasons (Lei et al., 2020; You et al., 2014). This may explain

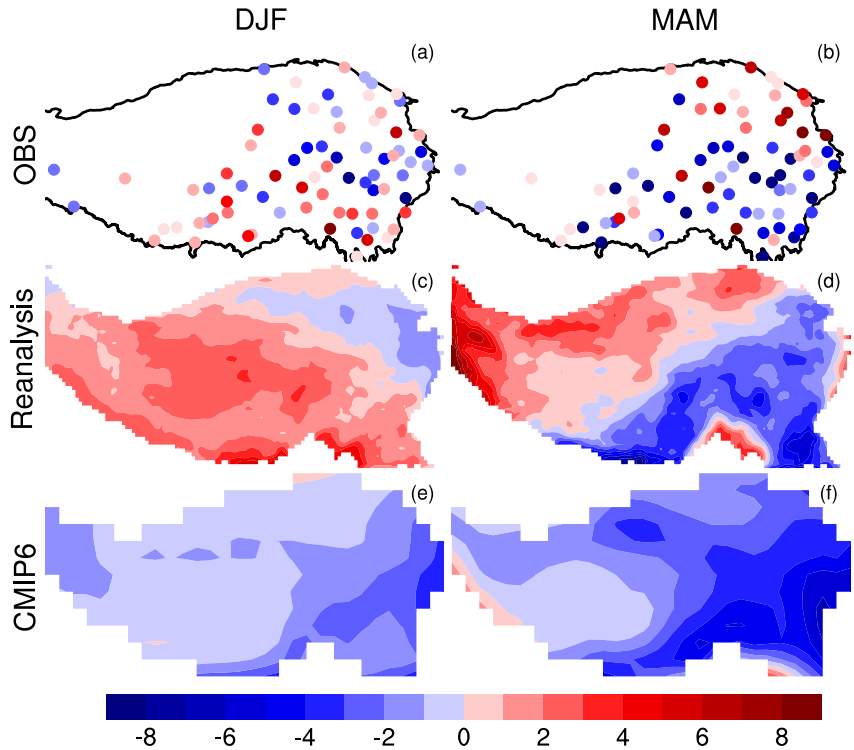

Figure 7. The spatial distributions of downward surface downward shortwave radiation change ($\Delta S^{\downarrow}$) from 1982–1998 to 1999–2015 in winter (DJF, left column) and spring (MAM, right column) for SunDu-derived data set at the 75 stations (a and b) and mean results of five reanalysis datasets (ERA5, MERRA, MERRA-2, JRA-55 and CRA) (c and d) and Coupled Model Intercomparison Project Phase 6 models (CMIP6) multi-model ensemble (e and f) over the entire Tibetan Plateau.

the positive $\Delta S^{\downarrow}$ over most area of TP in winter as shown for the reanalysis datasets. The decreasing $S^{\downarrow}$ over the southeastern TP and increasing $S^{\downarrow}$ over the other regions of TP in spring (Figures 7b and 7d) is in line with results from regional climate model simulations under the doubled CO_2 concentration scenario, in which the cloud amount increases at lower elevations and decreases at higher elevations in the eastern TP (Chen et al., 2003). There is large inter-model variation in the spatial distribution of $\Delta S^{\downarrow}$ over the TP for the CMIP6 models. The CMIP6 MME mean shows an overall decreasing $S^{\downarrow}$ over the TP in both winter and spring. However, the gradient of $\Delta S^{\downarrow}$ from the northwest to southeast of TP as represented in CMIP6 MME mean (Figures 7e and 7f) resembles that in reanalysis datasets during spring (Figure 7d). This spatial resemblance in the gradient but not the absolute values of $\Delta S^{\downarrow}$ for the CMIP6 models is likely due to their much coarser spatial resolution that cannot resolve the terrain gradients from western to eastern TP as well as do the reanalysis datasets with their higher spatial resolution.

3.4. SAF Contribution to TP Warming

Several studies have quantified the contribution of SAF to the surface temperature change over the TP (Gao et al., 2019; Ji et al., 2020; Su et al., 2017) using the perturbation form of surface energy budget equation. According to Equation 3, the contribution of SAF to surface temperature change (ΔT_{SAF}) over two climate periods is determined by four terms: (a) the sensitivity parameter $\left(-1/\left(4\sigma\overline{T_S}^3\right)\right)$ and (b) the surface downward solar radiation ($\overline{S^{\downarrow}}$) in the first climate period, (c) the surface albedo change ($\Delta\alpha$) and (d) surface downward solar radiation change ($\Delta S^{\downarrow}$) across the two climate periods. The magnitude of the sensitivity parameter is nearly the same for all six reanalysis datasets (Table S2 in Supporting Information S1), even though surface temperatures averaged over the 75 stations range from −15.4 K to −9.5 K in winter and from −2.0 to 2.9 K in spring. $\Delta S^{\downarrow}$ is two-orders of magnitude smaller than $\overline{S^{\downarrow}}$, therefore the magnitude of ΔT_{SAF} is mainly controlled by the sensitivity parameter,

$\overline{S^{\downarrow}}$ and $\Delta\alpha$. In the following, we compare the ΔT_{SAF} calculated for the 75 stations and the entire TP from the observational datasets, reanalysis datasets and CMIP6 models.

The 75-station averaged ΔT_{SAF} from the six reanalysis datasets is between −0.77 K (ERA-Interim) and 1.38 K (JRA-55) for winter, and between −0.84 K (ERA-Interim) and 1.73 K (ERA5) for spring. ERA-Interim presents a substantial cooling contribution of SAF (negative ΔT_{SAF}) in both winter and spring due to its significant surface albedo increases (Wu et al., 2020). JRA-55 presents the largest warming contribution of SAF (positive ΔT_{SAF}) in winter and ERA5 in spring due to their overestimated surface albedo reductions. To explore which item controls the inter-reanalysis spread in ΔT_{SAF}, Table S2 in Supporting Information S1 shows the coefficient of variation (CV) of the sensitivity parameter, $\overline{S^{\downarrow}}$, $\Delta S^{\downarrow}$ and $\Delta\alpha$ for the six reanalysis datasets, and $\Delta\alpha$ shows the largest CV magnitude. Therefore, the broad inter-reanalysis spread of ΔT_{SAF} can be attributed to the broad inter-reanalysis spread of surface albedo change.

The dominant role of $\Delta\alpha$ in determining the magnitude and spread of ΔT_{SAF} can be clearly illustrated by calculating ΔT_{SAF} for each reanalysis but substituting the reanalysis surface albedo with the satellite albedo (Table S2 in Supporting Information S1). In Table S2 in Supporting Information S1, $\Delta T_{SAF}^{CLARA-A2}$ and ΔT_{SAF}^{GLASS} show contributions of SAF to surface temperature change using $\Delta\alpha$ from the satellite products and other items of Equation 3 from the reanalysis datasets. The spread of $\Delta T_{SAF}^{CLARA-A2}$ reduces to between 0.20 and 0.22 K in winter and between 0.31 and 0.36 K for spring, similar reductions also occur for ΔT_{SAF}^{GLASS}. Consequently, the magnitudes of CV for $\Delta T_{SAF}^{CLARA-A2}$ and ΔT_{SAF}^{GLASS} are greatly reduced. The results of ΔT_{SAF} averaged over the entire TP higher than 2000 m a.s.l. are presented in Table S3 in Supporting Information S1. The averaged sensitivity parameters derived from the reanalysis datasets for the entire TP are very close to those averaged for the 75 stations. The ΔT_{SAF} of the entire TP exhibits as large a spread among the reanalysis datasets as that for the 75 stations, from −0.62 K (ERA-Interim) to 1.18 K (JRA-55) in winter and from −0.23 K (ERA-Interim) to 1.25 K (ERA5) in spring, the spread of ΔT_{SAF} is dominated by the spread of $\Delta\alpha$ as well. Similarly, using the two satellite-derived surface albedo changes over the TP, the spread of contributions of SAF to TP warming ($\Delta T_{SAF}^{CLARA-A2}$ and ΔT_{SAF}^{GLASS}) are significantly narrower than that of ΔT_{SAF} calculated directly from the six reanalysis datasets.

Equation 3 expresses a linear relationship between $\Delta\alpha$ and ΔT_{SAF}. Figure 8 explores this relationship by showing the averaged $\Delta\alpha$ and ΔT_{SAF} over the 75 stations and the entire TP for the six reanalysis datasets and CMIP6 models. One emergent feature of Figure 8 is that the six reanalysis datasets exhibit a strong, and very similar, linear relationships between the averaged $\Delta\alpha$ and ΔT_{SAF} for the 75 stations ($\Delta T_{SAF}^{lm(STN)} \sim \Delta\alpha$), and for the entire TP ($\Delta T_{SAF}^{lm(TP)} \sim \Delta\alpha$), meaning that the 75 stations do well represent the entire TP in terms of relationship between $\Delta\alpha$ and ΔT_{SAF}. Furthermore, the relationship derived from the CMIP6 models ($\Delta T_{SAF}^{lm(CMIP6)} \sim \Delta\alpha$) are very close to those from the reanalysis datasets, which suggests the CMIP6 models represent very similar SAF processes as the reanalysis datasets over the TP. The linear relationship between averaged $\Delta\alpha$ and ΔT_{SAF} shows great potential to be used to estimate ΔT_{SAF} in conjunction with the averaged $\Delta\alpha$ change from each data set. Table S4 in Supporting Information S1 compares the entire TP averaged ΔT_{SAF} calculated directly by Equation 3, $\Delta T_{SAF}^{lm(TP)}$ estimated from the linear regression between $\Delta\alpha$ and ΔT_{SAF} averaged for the entire TP, and $\Delta T_{SAF}^{lm(STN)}$ estimated from the linear regression between $\Delta\alpha$ and ΔT_{SAF} averaged for the 75 stations. The linear relationship of $\Delta\alpha$ and ΔT_{SAF} can predict the SAF contribution to the TP warming reasonably well, with an absolute difference less than 0.08 K (difference between ΔT_{SAF} and $\Delta T_{SAF}^{lm(TP)}$, ΔT_{SAF} and $\Delta T_{SAF}^{lm(STN)}$ in Table S4 in Supporting Information S1). These comparisons prove that the linear regressions between averaged $\Delta\alpha$ and ΔT_{SAF} over the 75 stations are accurate and can be used to estimate the ΔT_{SAF} for the entire TP.

To explain the representativeness of the 75 stations for the entire TP in terms of the relationship between $\Delta\alpha$ and ΔT_{SAF}, we apply a linear regression $\Delta T_{SAF} = \lambda \cdot \Delta\alpha + \varepsilon$ for the 75 stations and the grid cells of entire TP for each reanalysis data set (Figure 9). The linearly regressed relationships for the 75 stations are very close to that regressed for the grid cells of entire TP for each reanalysis data set, especially for winter. The difference in regression slopes (λ) for the 75 stations and the entire TP may result in different ΔT_{SAF} for a given $\Delta\alpha$, but quantitatively their impacts on ΔT_{SAF} is low because of the small magnitude of $\Delta\alpha$. Therefore, the linear relationship between $\Delta\alpha$ and ΔT_{SAF} derived from the 75 stations can well represent the entire TP, and this is a robust feature across the six reanalysis datasets and directly leads to the emergent feature presented in Figure 8. The linear regression formulas between $\Delta\alpha$ and ΔT_{SAF} shown in Figures 8 and 9 all have small residual terms that are insignificantly different from zero, which is consistent with Equation 3. According to Equation 3, the regression slope

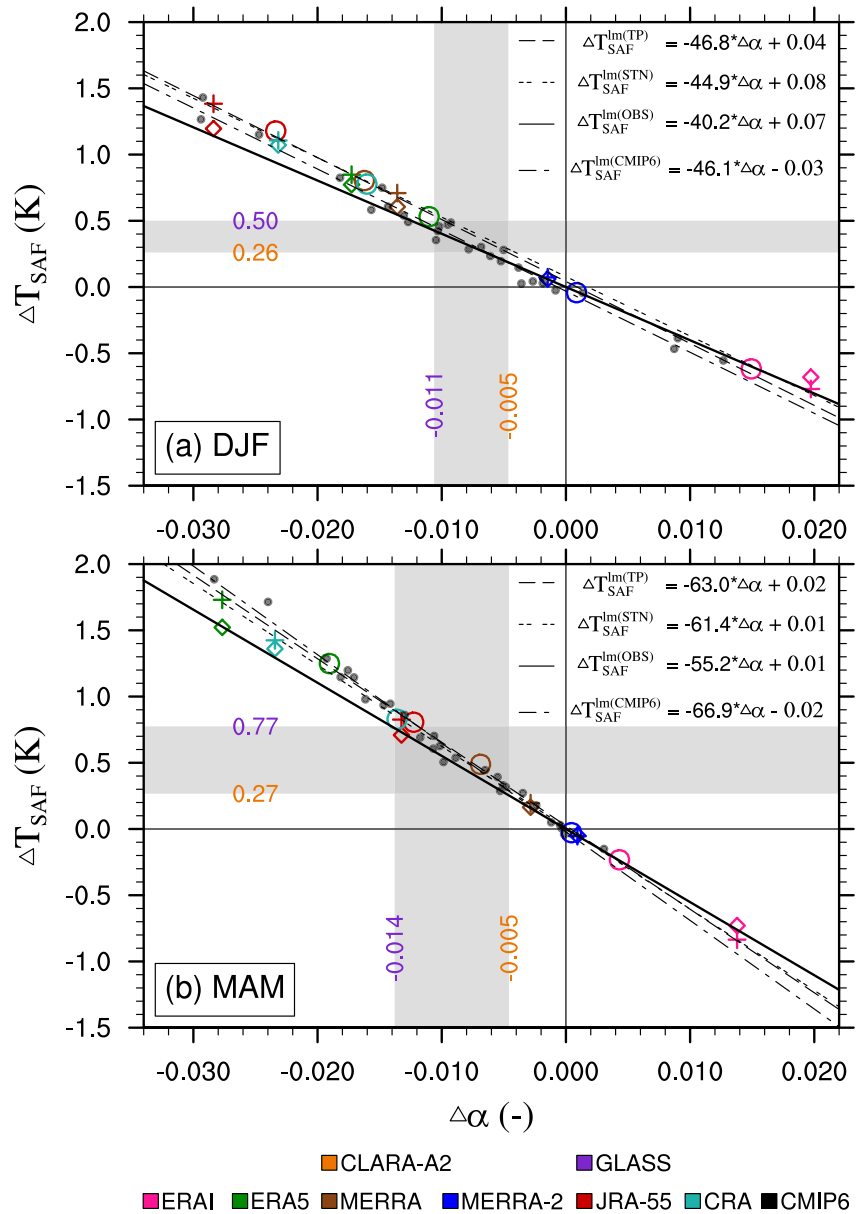

Figure 8. The linear regression between Δα and ΔT_{SAF} for winter (a) and spring (b). The circles markers denote the entire TP averaged Δα and ΔT_{SAF} for the six reanalysis datasets, the long-dash line is the linear regression for the six circle markers ($\Delta T_{SAF}^{lm(TP)} \sim \Delta\alpha$). The crosses markers denote the 75-station averaged Δα and ΔT_{SAF} for the six reanalysis datasets, the short-dash line is the linear regression for the six crosses markers ($\Delta T_{SAF}^{lm(STN)} \sim \Delta\alpha$). The diamonds markers denote the 75-station averaged Δα and ΔT_{SAF} for the six reanalysis datasets but using the SunDu-derived $S^{\downarrow}$, the solid black line is the linear regression for the six diamond markers ($\Delta T_{SAF}^{lm(OBS)} \sim \Delta\alpha$). The solid gray dot markers denote the entire Tibetan Plateau (TP) averaged Δα and ΔT_{SAF} for the Coupled Model Intercomparison Project Phase 6 (CMIP6) models, the long-short-dash line is the linear regression for the solid gray dot markers ($\Delta T_{SAF}^{lm(CMIP6)} \sim \Delta\alpha$). All linear regressions are significant at the 99.9% confidence level. The vertical gray band marks the uncertainty of the entire TP averaged surface albedo change above 2000 m a.s.l. based on CLARA-A2 and GLASS datasets, the horizontal gray band marks the corresponding range of ΔT_{SAF} according to the linear regression formula ($\Delta T_{SAF}^{lm(OBS)} \sim \Delta\alpha$).

(λ) represents a spatial averaging effect of $\lambda_i = \left(\overline{S^{\downarrow}} + \Delta S^{\downarrow}\right) / \left(4\sigma \overline{T_s}^3\right)$. The 75 stations can reasonably capture the statistical characteristics of λ_i for the entire TP, although most of the 75 stations are located over the central and eastern TP, and only few of them are located over the western TP. The representativeness of the 75 stations for the entire TP might be attributed to two reasons, (a) that the spatial inhomogeneity in surface temperature has

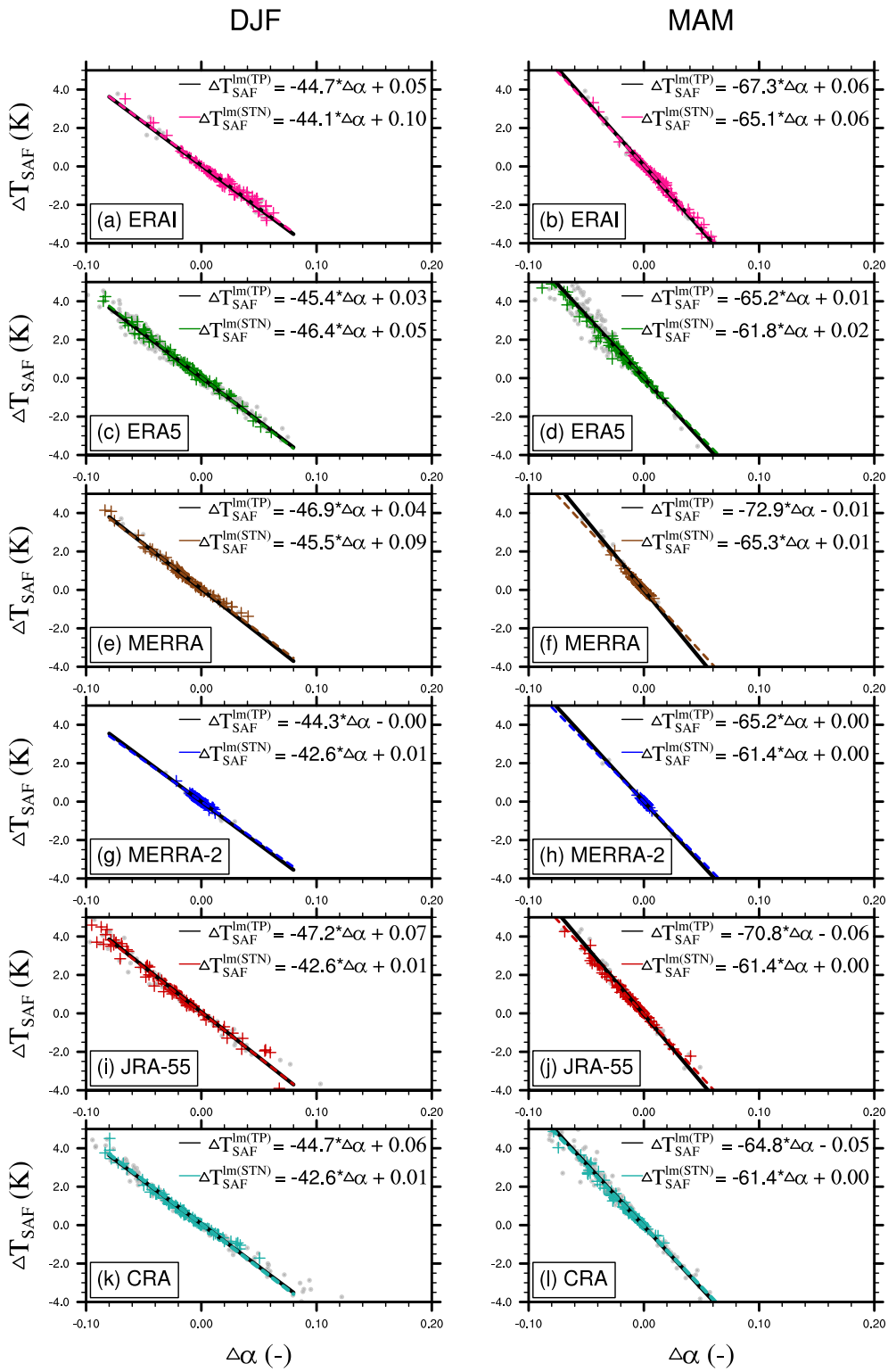

Figure 9. The linear regression between Δα and ΔT_{SAF} for the 75 stations (dashed colored lines and its corresponding formula $\Delta T_{SAF}^{lm(STN)} \sim \Delta\alpha$) and the entire Tibetan Plateau higher than 2000 m a.s.l. (solid black line and its corresponding formula $\Delta T_{SAF}^{lm(TP)} \sim \Delta\alpha$) of each reanalysis data set at winter (DJF, left column) and spring (MAM, right column). All linear regressions are significant at the 99.9% confidence level.

little effect on the spread of λ_i, and (b) that the multi-year average of $S^{\downarrow}$ tends to be relatively uniform due to the limited spatial horizon of the TP.

The regression slope between $\Delta\alpha$ and ΔT_{SAF} denotes the strength of SAF, that is how much surface temperature change responds to a unit change in surface albedo, and the strength of SAF mainly depends on the sensitivity parameter and $S^{\downarrow}$. Our previous analysis has shown that the sensitivity parameter is similar between datasets, therefore it is $S^{\downarrow}$ that moderates the strength of SAF over the TP. The reanalysis datasets and CMIP6 models overestimate the $S^{\downarrow}$ in winter and spring, therefore the strength of SAF in these datasets are overestimated as well. At the same time, the reanalysis datasets and CMIP6 models show varying biases in surface albedo change, which further enlarges the spread of estimated ΔT_{SAF} (Figure 8). To reduce the impacts of overestimated $S^{\downarrow}$ and varying biases in surface albedo change as represented in reanalysis datasets and CMIP6 models, the SunDu-derived $S^{\downarrow}$ at the 75 stations can be used to constrain the strength of SAF, and the surface albedo change from satellite products can be used to constrain the contribution of SAF to the TP surface warming. As the SunDu-derived $S^{\downarrow}$ and surface albedo change from satellite products are expected to be more reliable than the reanalysis and climate models over the TP, the observation constrained relationship between $\Delta\alpha$ and ΔT_{SAF} and surface albedo change should give a better estimation of the TP warming due to surface albedo change. Figure 8 shows that the regression slope of the observation constrained relationship between $\Delta\alpha$ and ΔT_{SAF} (solid line) is flatter than that directly regressed from the reanalysis datasets and CMIP6 models. In conjunction with the averaged surface albedo change over the 75 stations estimated from GLASS and CLARA-A2, the estimated ΔT_{SAF} is in the range of 0.23 K (CLARA-A2) to 0.55 K (GLASS) for winter, 0.29 K (CLARA-A2) to 0.56 K (GLASS) for spring, which is 14%–33% of the 75-station averaged surface warming for winter (1.66 ± 0.78 K) and 26%–50% of the 75-station averaged surface warming for spring (1.12 ± 0.61 K). In conjunction with the averaged surface albedo change over the entire TP, the estimated ΔT_{SAF} over the TP ($\Delta T_{SAF}^{lm(OBS)}$) is in the range of 0.26 K (CLARA-A2) to 0.50 K (GLASS) for winter, and 0.27 K (CLARA-A2) to 0.77 K (GLASS) for spring (Figure 8), which is slightly smaller than $\Delta T_{SAF}^{lm(STN)}$, $\Delta T_{SAF}^{lm(TP)}$ and $\Delta T_{SAF}^{lm(CMIP6)}$ given same surface albedo changes over the TP (Table S4 in Supporting Information S1). Hence, the linear relationship directly derived from the six reanalysis datasets tends to slightly overestimate the ΔT_{SAF} mainly due to its overestimated $S^{\downarrow}$. Since the range of surface albedo changes from CLARA-A2 and GLASS are treated as observational uncertainties, the corresponding range of estimated $\Delta T_{SAF}^{lm(OBS)}$ is considered as uncertainty for observation constrained contribution of SAF to the TP warming.

3.5. Revisiting Contributions of Climate Processes to TP Warming

The perturbation surface energy budget equation is used to decompose TP warming represented in the six reanalysis datasets and 28 CMIP6 models during the two climate periods, focusing on winter (DJF) and spring (MAM) when SAF is most important. The sums (ΔT_{SUM}) of the decomposed PTCs are very close to the surface temperature change (ΔT_S) represented by each reanalysis data set and CMIP6 model (Figure 10). The majority of the reanalysis datasets and CMIP6 models show SAF and clear-sky longwave heating are the two main contributing processes to the TP warming. Changes in cloud radiative forcing, clear-sky shortwave radiation and surface turbulent heat exchange mainly offset warming from SAF and clear-sky longwave heating. These cooling contributions are relatively stronger in most CMIP6 models than in the reanalysis datasets.

Most of the reanalysis datasets and CMIP6 models have their PTCs due to SAF (ΔT_{SAF}) outside the range of observation constrained SAF contribution to the TP warming (Figure 10). ERA5, CRA, MERRA and JRA-55 overestimate the SAF contribution to winter warming due to their overestimated surface albedo reduction and surface downward shortwave radiation (ΔT_{SAF} of 0.53 K, 0.78 K, 0.80 K and 1.18 K respectively). No reanalysis data set has winter ΔT_{SAF} within the observation constrained range of 0.26–0.50 K (Figure 10a). In spring, ERA5 largely overestimates the ΔT_{SAF} (1.25 K), and only MERRA has its ΔT_{SAF} (0.49 K) within the observation constrained range of 0.27–0.77 K. For the 28 CMIP6 models, the multi-model ensemble mean ΔT_{SAF} is 0.35 ± 0.47 K for winter and 0.64 ± 0.52 K for spring. Only 9 models in winter, and 12 models in spring have ΔT_{SAF} in the observation constrained range. Similar to ERA-Interim, five CMIP6 models (CMCC-CM2-SR5, FGOALS-g3, IITM-ESM, INM-CM5-0 and SAM0-UNICON) exhibit significant SAF cooling effects on the TP surface temperature change due to surface albedo increase, contrary to the surface albedo decrease in the two satellite products. In general, the spread of ΔT_{SAF} represented by the six reanalysis datasets is similar to that represented by the 28 CMIP6 models.

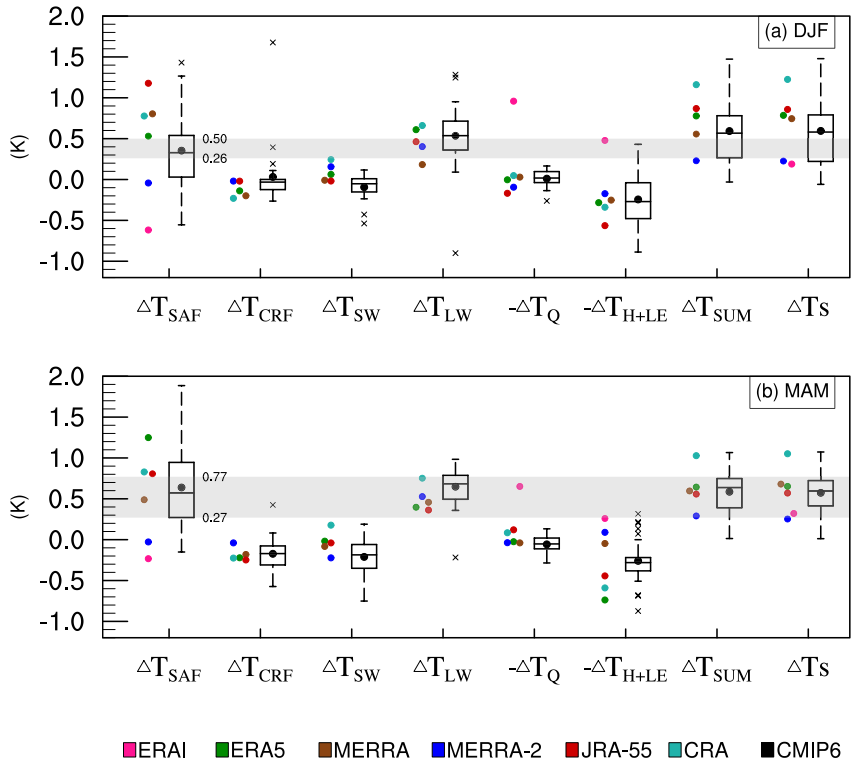

Figure 10. Surface partial temperature changes (PTCs) over the entire Tibetan Plateau (TP) higher than 2000 m a.s.l. decomposed by the perturbation surface energy budget equation for the six reanalysis datasets (colored solid dots) and 28 Coupled Model Intercomparison Project Phase 6 (CMIP6) models (boxplot) in winter (a) and spring (b) from 1982–1998 to 1999–2015. For the boxplot, each box represents the 25th and 75th percentiles (the interquartile range), the horizontal line in box represents the median, the ends of the whiskers represent the range of values falling within 1.5 inter-quartiles from the median, the outliers are marked as ×. Solid dot in boxplot represents the multi-model ensemble mean value. ΔT_{SAF} denotes PTC due to SAF, ΔT_{CRF} denotes PTC due to cloud radiative forcing, ΔT_{SW} denotes PTC due to downward clear sky shortwave radiation, ΔT_{LW} denotes PTC due to downward clear sky longwave radiation, ΔT_{Q} denotes PTC due to surface heat storage, ΔT_{H+LE} denotes PTC due to latent heat flux and sensible heat flux. ΔT_{SUM} denotes the summer of the six decomposed PTCs. ΔT_{S} denotes the total surface temperature change represented by reanalysis datasets. The horizontal gray zones indicate the observation constrained range of ΔT_{SAF} for the entire TP.

The spread of clear-sky longwave heating effect on the TP warming (ΔT_{LW}) is much narrower than ΔT_{SAF} both for the reanalysis datasets and CMIP6 models. Previous studies (Gao et al., 2019; Su et al., 2017) conclude that SAF generally contributes more to the TP warming than does the clear-sky longwave heating. However, this is not valid for many reanalysis datasets and CMIP6 models analyzed here when considering the observational constraints on the contribution of SAF to the TP warming. In winter, ERA5, CRA and most CMIP6 models have their ΔT_{LW} larger than the observation constrained ΔT_{SAF}, JRA-55 and MERRA-2 have their ΔT_{LW} within the observation constrained range of ΔT_{SAF}, and MERRA shows much weaker contribution of clear-sky longwave heating. In spring, all six reanalysis datasets and most of CMIP6 models have their ΔT_{LW} within the observation constrained range of ΔT_{SAF}. The reanalysis datasets and CMIP6 models tend to suggest the clear-sky longwave heating is more important in winter TP warming, while the SAF and the clear-sky longwave heating are of equal importance in spring TP warming. The important role of clear-sky longwave heating in winter TP warming is more robust for CMIP6 models that simulate TP warming close to observation.

Reanalysis datasets of successive generations from the same data center might suggest different climate process dominating the TP warming. ERA-Interim shows surface heat storing and surface turbulence heat exchanging are the main processes warming the TP, while SAF exerts a significant cooling effect to counteract the TP warming, especially during winter. Wu et al. (2020) draw a similar conclusion for ERA-Interim in winter using the CFRAM. ERA5 shows SAF and clear-sky longwave heating are main processes warming the TP in winter, and SAF is the main process warming the TP in spring. For ERA5, the contribution of change in surface heat storage to the TP warming is negligible, and turbulent heat exchanging counteracts part of the TP warming, especially

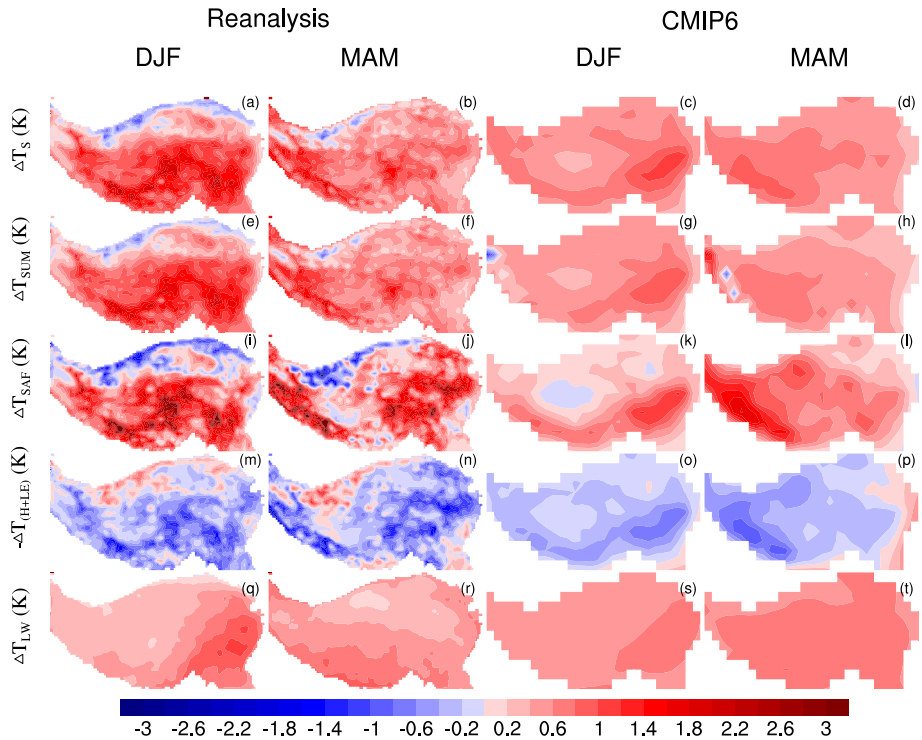

Figure 11. The spatial distributions of ΔT_S (a–d), ΔT_{Sum} (e–h), ΔT_{SAF} (i–l), $-\Delta T_{(H+LE)}$ (m–p), and ΔT_{LW} (q–t) from 1982–1998 to 1999–2015 in winter (DJF) and spring (MAM) for mean results of five reanalysis datasets (ERA5, MERRA, MERRA-2, JRA-55 and CRA) (left two columns) and Coupled Model Intercomparison Project Phase 6 (CMIP6) multi-model ensemble (right two columns) over the Tibetan Plateau.

during spring. MERRA and MERRA-2 show very different contributions of SAF to the TP warming as well. MERRA shows relatively strong warming contribution of SAF to the TP warming, while MERRA-2 shows a weak cooling contribution of SAF. For MERRA-2, clear-sky longwave heating process dominates the TP warming both for winter and spring, and the ΔT_{LW} is within the observation constrained range of ΔT_{SAF}. However, Ji et al. (2020) found MERRA-2 fails to capture the accelerated winter TP warming during recent decades. The evolving and inconsistent contribution of SAF to the TP warming represented in different generations of reanalysis datasets indicates large uncertainties in the reanalysis datasets over the TP.

Figure 10 presents a strong compensating effect between ΔT_{SAF} and $-\Delta T_{(H+LE)}$. It is especially clear in the six reanalysis datasets, JRA-55 shows strongest positive ΔT_{SAF} and strongest negative $-\Delta T_{(H+LE)}$ while ERA-Interim shows strongest negative ΔT_{SAF} and strongest positive $-\Delta T_{(H+LE)}$ during winter, similar contrast occurs for ERA5 and ERA-Interim in spring. The uncertainty of ΔT_{SAF} is mainly caused by differences in surface albedo changes ($\Delta\alpha$) among datasets. The uncertainty of $-\Delta T_{(H+LE)}$ in the reanalysis datasets comes from both sensible heat flux and latent heat flux, while for the CMIP6 models the uncertainty of $-\Delta T_{(H+LE)}$ is mainly from sensible heat flux (not shown). The uncertainty of sensible heat flux and latent heat flux may be attributed to gradients in land-air temperature and humidity and near surface wind. Both the reanalysis datasets and CMIP6 models show low consensus on ΔT_{SAF} and $-\Delta T_{(H+LE)}$ due to their relatively large inter-model spread. However, the spread of their sum ($\Delta T_{SAF-(H+LE)}$) is considerably smaller than that of ΔT_{SAF} and $-\Delta T_{(H+LE)}$ (Table S5 in Supporting Information S1), as models may have compensating biases when simulating the various components of the surface energy budget (Boeke & Taylor, 2016; Liu et al., 2021) and this manifests in their contribution to surface temperature change. For the reanalysis datasets and CMIP6 models overestimating the contribution of SAF to surface warming, the opposite contribution from the turbulent heat fluxes tends to be overestimated as well. Therefore, using the observations to constrain the uncertainty of ΔT_{SAF} would contribute to reducing the uncertainty of turbulent heat fluxes.

Figure 11 shows the spatial distributions of ΔT_S, ΔT_{SUM} and three main PTCs contributing to the TP temperature change: ΔT_{SAF}, $-\Delta T_{(H+LE)}$ and ΔT_{LW} from the mean results of reanalysis datasets and CMIP6 models. As

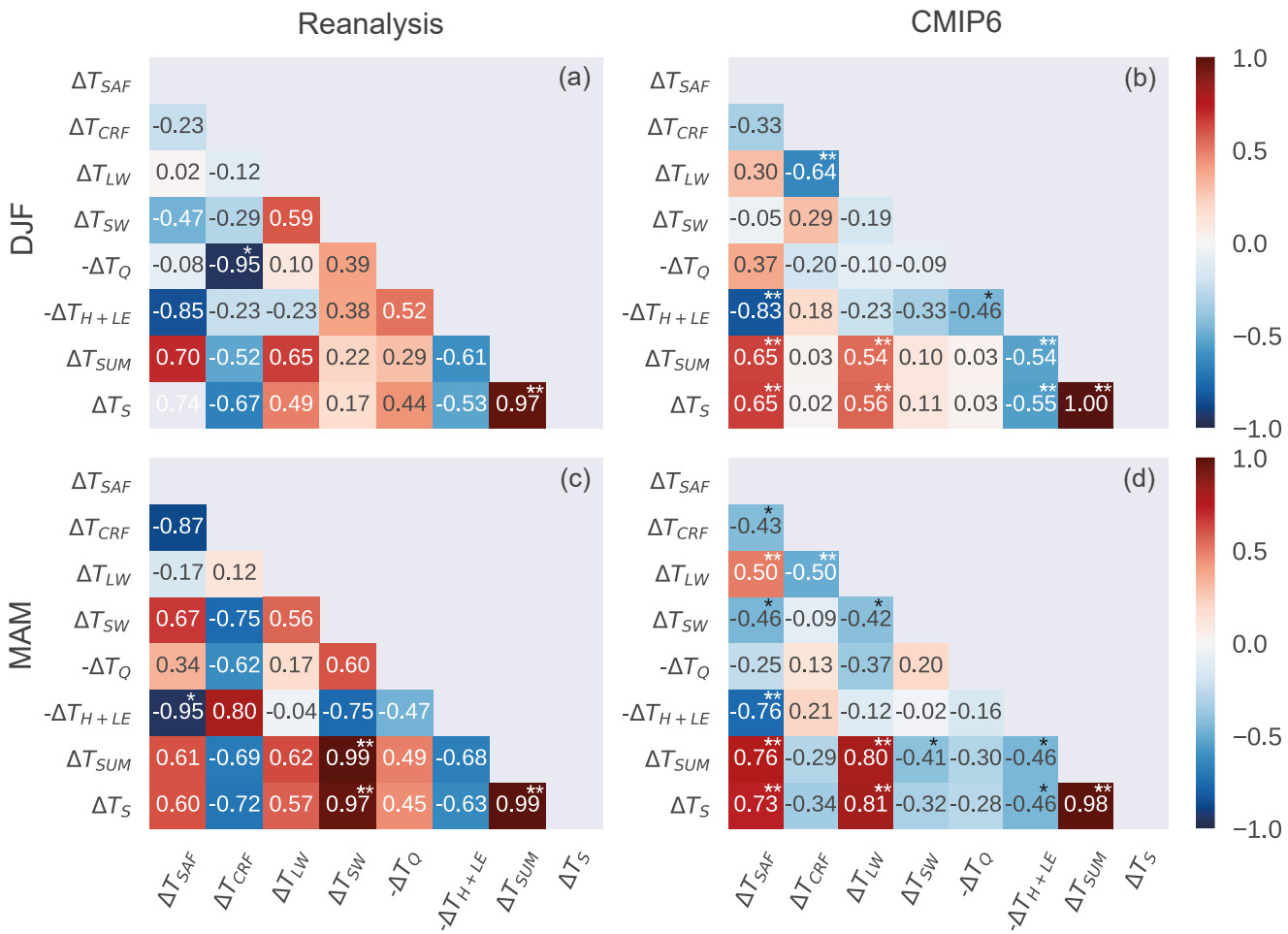

Figure 12. The correlation coefficient matrix of the partial temperature changes decomposed by the perturbation surface energy budget equation for five reanalysis datasets (ERA5, MERRA, MERRA-2, JRA-55, CRA) and 28 Coupled Model Intercomparison Project Phase 6 (CMIP6) models in winter (a and b) and spring (c and d). Colors and numbers in each cell correspond to color bar (*: significant at $p < 0.05$, **: significant at $p < 0.01$).

ERA-Interim lacks clear-sky fields and its ΔT_{LW} can not be calculated directly, only five reanalysis datasets are included for analysis. The similar spatial distribution of the characteristics of the ΔT_S and ΔT_{SUM} in the reanalysis datasets and CMIP6 models (except for several grid cells in the northwestern TP) confirm the reliability of linear decomposition of the perturbation surface energy budget equation over the TP. In CMIP6 models, the obvious difference between ΔT_S and ΔT_{SUM} for several grid cells in the northwestern TP comes from EC-Earth3-AerChem and EC-Earth3-CC models, which might be due to some imbalance in their surface energy budget where snow is thick. Both the reanalysis multi-dataset mean and CMIP6 multi-model mean show more winter warming occurs in the southeastern TP, controlled mainly by SAF and clear-sky longwave heating effects, and more spring warming occurs in the southwestern TP controlled mainly by SAF effects. The outstanding warming over the southwestern TP, especially the warming over the Himalayas, has been primarily attributed to the SAF strengthened by black carbon (Ma et al., 2019). The spatial distributions of ΔT_{SAF} and $-\Delta T_{(H+LE)}$ are highly anti-correlated, the cooling effects of the turbulent heat fluxes compensates a large part of the warming effects due to SAF, and is notable over the southwestern and southeastern TP. Over the northern TP, the cooling effect due to surface albedo increase is also compensated by the warming effect from turbulent heat fluxes. In general, the spatial variation of clear-sky longwave heating effects (ΔT_{LW}) is smaller than ΔT_{SAF} and $-\Delta T_{(H+LE)}$, as ΔT_{LW} is mainly attributed to uniform changes in atmospheric CO_2 concentration and variations in regional water vapor and terrain height.

Figure 12 shows the matrix of correlation coefficients between pairs of PTCs decomposed by the perturbation surface energy budget equation in five of the six reanalysis datasets and 28 CMIP6 models in winter and spring.

The ERA-Interim is excluded in the matrix analysis here due to its lack of ΔT_{CRF}, ΔT_{LW} and ΔT_{SW}. ΔT_{SUM} and ΔT_S are highly correlated, indicating the reliability of the decomposition of the perturbation surface energy budget equation. The CMIP6 models show that TP warming (ΔT_S, ΔT_{SUM}) is significantly ($p < 0.01$) correlated with ΔT_{SAF}, ΔT_{LW}, and $-\Delta T_{H+LE}$ in winter and spring (Figures 12b and 12d), but they are not significant for the five reanalysis datasets (Figures 12a and 12c). We note that when using all six reanalysis datasets, the TP warming is significantly correlated with ΔT_{SAF} in winter and spring ($p < 0.05$). The SAF induced warming explains 55% (winter) and 36% (spring) of the TP warming variation in reanalysis datasets, and 44% (winter) and 56% (spring) of the TP warming in CMIP6 models.

The significant positive correlation between ΔT_S and ΔT_{SAF}, and significant negative correlation between ΔT_S and $-\Delta T_{H+LE}$ directly results from surface energy balance as SAF leads to change in surface energy input and the land surface balances it through changes in turbulent heat fluxes. The anticorrelation between ΔT_{SAF} and $-\Delta T_{H+LE}$ can be as high as -0.95 for reanalysis datasets in spring and -0.83 for CMIP6 models in winter. The joint effect of SAF and turbulent heat fluxes on the TP warming is about half of the standalone SAF contribution to the TP warming as shown in Table S5 in Supporting Information S1, reflecting their compensating effects as discussed earlier. Therefore, reasonable representation of SAF processes in reanalysis systems and climate models is necessary to reproduce the historical TP warming and it would help reduce the uncertainties in surface turbulent heat fluxes as well.

The significant positive correlation between ΔT_S and ΔT_{LW} directly results from increased greenhouse gases. Figure 12 shows a significant negative correlation between ΔT_{LW} and ΔT_{CRF} for CMIP6 models in both winter and spring. This seems to imply a negative correlation between ΔT_S and ΔT_{CRF}, but it is only true for CMIP6 models in spring with relatively broad spread of ΔT_{CRF} (Figure 12d), not in winter with relatively narrow spread of ΔT_{CRF} (Figure 12b). The spread of ΔT_{LW} among CMIP6 models can be mostly attributed to varying changes in atmospheric water vapor content resulting from differences in water vapor feedback and regional atmospheric circulation change, as the CMIP6 models are specified with the same anthropogenic greenhouse gas concentrations for the AMIP simulations analyzed here. Higher atmospheric water vapor content tends to produce more clouds and negative contributions to shortwave cloud radiative forcing on the surface temperature change over the TP, and this is manifested as a negative correlation between ΔT_{LW} and ΔT_{CRF}.

Due to the small number of reanalysis data set samples, the correlations presented in Figures 12a and 12c should be interpreted with caution. For example, the significantly high correlation between ΔT_{CRF} and $-\Delta T_Q$ in winter (Figure 12a) presented in the five reanalysis datasets, but not in the CMIP6 models. Both ΔT_{CRF} and $-\Delta T_Q$ play small roles in TP surface temperature change and their roles in TP winter warming are inconsistent in the reanalysis datasets, as well as in CMIP6 models. The reanalysis datasets also present a significantly high correlation between ΔT_{SW} and ΔT_S in spring (Figure 12c), which might suggest less decline in $S^{\downarrow}$ is in line with more TP surface warming, this reflects varying performance of the reanalysis datasets on reproducing the declining trend of $S^{\downarrow}$ in observations.

4. Discussion and Conclusion

The amplified TP warming is an issue of wide scientific concern. Previous studies (Gao et al., 2019; Ji et al., 2020; Su et al., 2017; Wu et al., 2020) attribute the surface warming amplification over the TP in winter and spring to SAF, clear-sky longwave heating and heat storage changes. However, we find that the fidelity of surface albedo and surface downward shortwave radiation in reanalysis datasets, which directly affect the contribution of SAF to the TP surface temperature changes is suspect.

The state-of-the-art reanalysis datasets and CMIP6 climate models exhibit varying biases in surface albedo over the TP compared with the satellite products CLARA-A2 and GLASS. In terms of climatology, ERA-Interim, ERA5, JRA-55 and CRA significantly overestimate the surface albedo in winter and spring. MERRA overestimates the climatological albedo over the TP to a lesser extent and MERRA-2 shows the best climatology compared with the satellite surface albedo products. Most CMIP6 models also overestimate the TP surface albedo, with just a few models close to the observations. Li et al. (2016) found that systematic overestimation of surface albedo in climate models results in cold temperature bias in the Northern Hemisphere, especially at high altitudes. The cold biases over the TP in previous generations of climate models and reanalysis datasets has also been noted by Chen et al. (2017) and Yan et al. (2020). Therefore, we may expect that the systematic

overestimation of TP surface albedo in recently published reanalysis datasets and CMIP6 models should result in cold biases over the TP as well.

CLARA-A2 and GLASS show that the surface albedo changes averaged over the TP between the two consecutive climatic periods are in the range of −0.005 to −0.014 for winter and spring. The CLARA-A2 data set presents smaller averaged surface albedo changes over the TP than the GLASS data set in both winter and spring. Satellite surface albedo datasets over the TP could be biased due to the similar optical characteristics of snow cover, ice and cloud, complex topography and uncertainties in inversion algorithms (An et al., 2020; Chen et al., 2017; Shi & Liang, 2013a). Systematic biases that are constant over time will have no impact on the surface albedo change over two consecutive climate periods. If biases vary over time, then changes over specific periods will be affected. However, scarcity of long-term validation data does not allow us to assess the uncertainties of the estimated surface albedo change directly.

Surface albedo change is highly correlated with snow cover change over the TP both spatially and temporally (Chen et al., 2017; Pang et al., 2022; Shi & Liang, 2013b), the changes of surface albedo in cold season are mainly driven by snow cover change. Observations of TP snow cover vary spatially, for example, a significant increasing trend in the central-eastern area, and a significant decreasing trend in the southern area in winter and spring (Wang et al., 2018), which are consistent with varying top of atmosphere radiative forcing (Flanner et al., 2011). The spatially different snow cover change tends to produce small changes in area- and time-averaged surface albedo. However, the CLARA-A2 surface albedo data set shows substantially smaller differences over the two climate periods than does the GLASS data set. The cloud masking procedure applied in the CLARA-A2 surface albedo production (Karlsson et al., 2017) might affect its long-term trend of surface albedo as the station observations and satellite datasets show decreasing trends in cloud cover over the TP (Duan & Wu, 2006; Lei et al., 2020). More snow surface being exposed under decreasing cloud cover change could lead to the smaller change in surface albedo derived from the CLARA-A2 data set during the historical period. This is consistent with the percentage of masked grid cells of the CLARA-A2 surface albedo data set decreasing from 13.2% to 2.5% for winter and spring during the two climate periods over the TP. A previous study also found the decreasing trend of CLARA-A2 surface albedo over the TP during the period 2001–2015 is about three times smaller than that from the MODIS surface albedo data set (Pang et al., 2022), which has been validated extensively and widely used as a benchmark for evaluating satellite albedo datasets (He et al., 2014). If this artificially weakened declining trend of CLARA-A2 holds true for the two climate periods in this study, the lower bounds of constrained SAF contribution to TP warming would be underestimated when derived from the CLARA-A2 data set.

Assuming the snow cover change dominates the surface albedo change over the TP, especially during cold seasons, then surface albedo differences over the two climate periods can be simply estimated from the surface snow cover change over the two climate periods and the seasonal sensitivity of surface albedo change to snow cover change. To evaluate the uncertainty of GLASS surface albedo change over the entire TP, we use an independent data set to derive the seasonal sensitivity of surface albedo change to snow cover change: a daily snow depth product derived from the passive microwave remote sensing datasets with validation by CMA station observations (Che & Dai, 2015; Che et al., 2008; Dai et al., 2015), with an empirical equation (Wu & Wu, 2004) to transform snow depth to snow cover fraction. Passive microwave remote sensing has better cloud penetration and provides snow layer and surface information and high temporal resolution, and is an efficient approach to derive snow depth or snow water equivalent. As snow cover retreats and affects surface albedo mainly in spring, we consider two month-to-month transitions (from March to April and from April to May) to obtain multi-year mean month-to-month changes in snow cover fraction and surface albedo. For the entire period 1982–2015, the estimated mean month-to-month snow cover fraction change is -0.077 ± 0.024, and the corresponding mean month-to-month surface albedo change is -0.018 ± 0.003. Then the derived seasonal sensitivity of surface albedo change to snow cover fraction change is 0.257 ± 0.007. The decrease in snow cover fraction averaged over the TP is 0.048 and 0.038 for winter and spring respectively during the two climate periods, hence the estimated surface albedo change is -0.012 ± 0.003 and -0.010 ± 0.003 for winter and spring respectively, which are well close to the surface albedo changes directly calculated from the GLASS: −0.011 and −0.014 for winter and spring respectively.

Compared with two satellite surface albedo products, JRA-55 significantly overestimates the surface albedo reduction in winter, ERA5 significantly overestimates the surface albedo reduction in spring. CRA overestimates the surface albedo reduction but to a lesser extent. ERA-Interim exhibits a notable albedo increase both in winter

and spring, MERRA-2 exhibits weakest albedo change and underestimates the surface albedo change. CRA, JRA-55 and MERRA have their surface albedo reductions within the observational range over the TP in spring. The CMIP6 MME mean surface albedo change averaged over the TP is within the range given by the two satellite products. The spread of surface albedo change in CMIP6 models is comparable to that of the six reanalysis datasets. The six analysis datasets do not show obvious advantages over the CMIP6 models in representing the TP surface albedo change. Biases in surface albedo changes affect surface radiation budget and exert influences on local and even remote climate (Thackeray et al., 2019), and these influences are partially manifested through SAF (Qu & Hall, 2014).

All six reanalysis datasets overestimate the averaged surface downward shortwave radiation compared with the ground measurements and SunDu-derived $S^{\downarrow}$. The averaged $S^{\downarrow}$ biases in the reanalysis datasets can be as large as 28.7 W/m^2 in winter and 50.8 W/m^2 in spring compared with the ground measurements. Most CMIP6 models have their $S^{\downarrow}$ closer to the ground measurements than the reanalysis datasets. This might be due to coarser horizontal resolution of CMIP6 models than that of reanalysis datasets, land surface grid cells of coarser horizontal resolution over the TP tend to be of lower altitude and receive less downward shortwave radiation due to stronger atmospheric attenuation. The overestimated $S^{\downarrow}$ results in relatively overestimated SAF warming contribution, given the same surface albedo change. However, our results show that the coefficient of variation of surface albedo change is much larger than that of $S^{\downarrow}$ among the reanalysis datasets. The spread of surface albedo change is the major factor determining the spread of contributions of SAF to the TP warming represented by the reanalysis datasets and CMIP6 models.

Six state-of-the-art reanalysis datasets and CMIP6 models reveal a strong linear relationship between surface albedo change ($\Delta\alpha$) and corresponding surface temperature change (ΔT_{SAF}) over the TP. The linear relationship between $\Delta\alpha$ and ΔT_{SAF} holds true both for 75 observation stations and the entire TP, and the linear relationship derived from the 75 stations can well represent the entire TP. To reduce the impacts of overestimated $S^{\downarrow}$ in the reanalysis datasets and CMIP6 models, the SunDu-derived $S^{\downarrow}$ is used to constrain the relationship between $\Delta\alpha$ and ΔT_{SAF}. Using the observation constrained linear relationship between $\Delta\alpha$ and ΔT_{SAF} in conjunction with surface albedo change from two satellite products, the estimated contribution of SAF to the TP warming over recent decades is in the range of 0.26–0.50 K for winter and 0.27–0.77 K in spring. The contribution of SAF to the TP surface temperature change directly estimated by Equation 3 from the six reanalysis datasets are in the range of −0.62 to 1.18 K for winter, and −0.23 to 1.25 K for spring. The observation constrained relationship between $\Delta\alpha$ and ΔT_{SAF} significantly reduces the uncertainties in estimating the contribution of SAF to the TP warming.

TP topography is complex; climatic characteristics between western and eastern TP are different; western TP usually receives more surface downward shortwave radiation than eastern TP, while observation stations are usually in valleys near towns in eastern TP, raising doubts on the appropriateness of extending station observations to the entire TP (Yang et al., 2008). However, the linear relationship between $\Delta\alpha$ and ΔT_{SAF} derived from the 75 stations are representative of the $\Delta\alpha$ and ΔT_{SAF} relationship for the entire TP to good accuracy. The difference in estimated ΔT_{SAF} from the 75 stations is less than 0.08 K for the reanalysis datasets, this difference tends to be overestimated considering the overestimated $S^{\downarrow}$ in the reanalysis datasets. The bias in ΔT_{SAF} due to the representativeness of the 75 stations is much smaller than the range of estimated ΔT_{SAF} due to uncertainty in $\Delta\alpha$ inferred from satellite products, which is about 0.24 K for winter and 0.50 K for spring. Our study suggests the inhomogeneity of surface downward shortwave radiation over the TP is a minor contributor in estimated SAF effects, while the surface albedo change related to snow cover change dominates the discrepancy in ΔT_{SAF}.

The observation constrained SAF contribution to the TP surface temperature change provides an opportunity to revisit the dominant factor determining the amplified warming over TP. Most of the reanalysis datasets and CMIP6 models have their PTCs due to SAF (ΔT_{SAF}) outside the range of observation constrained SAF contribution to the TP warming. CMIP6 MME mean ΔT_{SAF} is within the observation constrained range for both winter and spring. Four of the six reanalysis datasets (CRA, ERA5, MERRA and JRA-55) and most CMIP6 climate models suggest the SAF and clear-sky longwave heating are the two main climate processes contributing to the amplified TP warming in winter and spring, consistent with previous studies (Gao et al., 2019; Ji et al., 2020; Su et al., 2017). The warming contribution due to clear-sky longwave heating tends to be stronger than the observation constrained contribution of SAF in winter and consistent with them in spring. The reanalysis datasets and CMIP6 models tend to suggest the clear-sky longwave heating is more important in winter warming, while the SAF and the clear-sky longwave heating are of equal importance in spring warming. The six reanalysis datasets

and CMIP6 models show significant correlation between ΔT_{SAF} and the TP warming, the SAF induced warming explains about half of the TP warming variations in the reanalysis datasets and CMIP6 models. The strong anticorrelation between ΔT_{SAF} and $-\Delta T_{H+LE}$ indicates a strong compensating effect between the contributions of SAF and turbulent heat exchanging to the amplified TP warming. The spread of their joint contribution to TP warming is considerably smaller than that of ΔT_{SAF} and $-\Delta T_{(H+LE)}$. Therefore, reasonable representation of SAF processes in reanalysis systems and climate models is necessary to reproduce the historical TP warming and it would help reduce the uncertainties in surface turbulent heat fluxes as well.

Reanalysis datasets have assimilated available surface and upper air observations and have complete spatial coverage, they are widely used in the climate change studies. Due to scarcity of observational data set over the TP, atmospheric reanalysis is less well constrained over the TP than many other regions. The complex topography of the TP and associated energy and moisture flows produce a unique climatology that is difficult to simulate in reanalysis modeling systems (Bian et al., 2020; Orsolini et al., 2019; Yan et al., 2020). Of the six reanalysis datasets used in our study, ERA5 and MERRA-2 are evolving and directly supersede ERA-Interim and MERRA, but display opposite SAF effects over the TP. Biases in the reanalysis datasets contribute to a low consensus on the TP amplified warming mechanism when diagnosed purely from the reanalysis. On the other hand, the CMIP6 multi-model ensemble mean behavior is relatively closer to the observations over the TP. The state-of-the-art reanalysis datasets, despite higher spatial resolution, exhibit no obvious advantages over the CMIP6 models in representing SAF over the TP. Our study emphasizes the importance of using available observations to constrain reanalysis datasets and climate models over the TP, and the importance of process-based evaluation of the reanalysis datasets and climate models. The surface albedo biases in the reanalysis datasets affect surface energy budgets, which should lead to caution when interpreting TP climate change purely based on reanalysis datasets. Improving the quality of reanalysis datasets requires both more in situ observations and improvements in model parameterization schemes.

Data Availability Statement

The observed daily ground surface temperature data is available from CMA at http://101.200.76.197/data/dtail/dataCode/SURF_CLI_CHN_MUL_DAY_V3.0.html. The ground measurements of surface downward shortwave radiation are available from CMA at https://data.cma.cn/data/cdcdetail/dataCode/RADI_MUL_CHN_DAY.html. The long-term series of daily snow depth data set in China is available from the National TP Data Center (TPDC) at http://data.tpdc.ac.cn/zh-hans/data/df40346a-0202-4ed2-bb07-b65dfcda9368/. The CLARA-A2 surface albedo product is available from the Satellite Application Facility on Climate Monitoring (CM SAF) at https://wui.cmsaf.eu/safira/action/viewProduktDetails?fid=18&eid=21707. The GLASS surface albedo product is available from National Earth System Science Data Center at http://www.geodata.cn/data/index.html?word=GLASS%20albedo. The SunDu-derived surface incident solar radiation data is provided by He et al. (2018) at https://doi.org/10.1029/2018GL077424. The ERA-Interim reanalysis data set is available from ECMWF at https://apps.ecmwf.int/datasets/data/interim-mdfa/levtype=sfc/. The ERA5 reanalysis data set is available from ECMWF at https://cds.climate.copernicus.eu/cdsapp#!/dataset/reanalysis-era5-single-levels-monthly-means?tab=form. The MERRA reanalysis data set is available from NASA Modeling and Assimilation Dara and Information Services Center (MDISC) at https://disc.gsfc.nasa.gov/datasets/MAT1NXRAD_5.2.0/summary. The MERRA-2 reanalysis data set is available from NASA MDISC at https://disc.gsfc.nasa.gov/datasets/M2T1NXRAD_5.12.4/summary. The JRA-55 reanalysis data set is available from the Japan Meteorological Agency (JMA) at https://rda.ucar.edu/datasets/ds628.0/. The CRA reanalysis data set is available from China Meteorological Data Service Center at https://data.cma.cn/data/cdcdetail/dataCode/NAFP_CRA40_FTM_MON.html. The CMIP6 models' outputs are available from the Earth System Grid Federation at https://esgf-node.llnl.gov/projects/cmip6/.

Acknowledgments
The authors thank the relevant organizations and teams for providing the datasets used in this study and the Super Computing Center of Beijing Normal University for providing computing resources. This study is supported by National Key R&D Program of China (No. 2017YFA0603603) and National Nature Science Foundation of China (No. 41875126). The authors would like to thank the reviewers for their thoughtful comments and efforts towards improving our manuscript. The authors would like to thank Dr. Qiang Liu and Dr. Xihan Mu for their helpful discussions.

References

An, Y., Meng, X., Zhao, L., Li, Z., Wang, S., Shang, L., et al. (2020). Performance of GLASS and MODIS Satellite Albedo products in diagnosing Albedo variations during different time scales and special weather conditions in the Tibetan Plateau. *Remote Sensing*, *12*(15). https://doi.org/10.3390/RS12152456

Basang, D., Barthel, K., & Olseth, J. (2017). Satellite and ground observations of snow cover in Tibet during 2001–2015. *Remote Sensing*, *9*(11), 1201. https://doi.org/10.3390/rs9111201

Beijing Normal University/China. (2013). GLASS: Long-term GLASS Albedo product [Dataset]. Research Data Archive at the National Earth System Science Data Center, National Science & Technology Infrastructure of China. https://doi.org/10.12041/geodata.GLASS_Albedo_avhrr.ver1.db

Bian, Q., Xu, Z., Zheng, H., Li, K., Liang, J., Fei, W., et al. (2020). Multiscale changes in snow over the Tibetan plateau during 1980–2018 represented by reanalysis data sets and satellite observations. *Journal of Geophysical Research: Atmospheres*, *125*(19), 0–3. https://doi.org/10.1029/2019JD031914

Boeke, R. C., & Taylor, P. C. (2016). Evaluation of the Arctic surface radiation budget in CMIP5 models. *Journal of Geophysical Research: Atmospheres*, *121*, 8525–8548. https://doi.org/10.1002/2016JD025099

Bosilovich, M., Akella, S., Coy, L., Cullather, R., Draper, C., Gelaro, R., et al. (2015). MERRA-2: Initial evaluation of the climate. *NASA Technical Report Series on Global Modeling and Data Assimilation*, *43*, 139.

Brown, R. D., & Derksen, C. (2013). Is Eurasian October snow cover extent increasing? *Environmental Research Letters*, *8*(2). https://doi.org/10.1088/1748-9326/8/2/024006

Cai, M., & Lu, J. (2009). A new framework for isolating individual feedback processes in coupled general circulation climate models. Part II: Method demonstrations and comparisons. *Climate Dynamics*, *32*, 887–900. https://doi.org/10.1007/s00382-008-0424-4

Che, T., & Dai, L. (2015). Long-term series of daily snow depth dataset in China (1979–2021) [Dataset]. National Tibetan Plateau Data Center. https://doi.org/10.11888/Geogra.tpdc.270194

Che, T., Li, X., Jin, R., Armstrong, R., & Zhang, T. (2008). Snow depth derived from passive microwave remote-sensing data in China. *Annals of Glaciology*, *49*(1), 145–154. https://doi.org/10.3189/172756408787814690

Chen, B., Chao, W. C., & Liu, X. (2003). Enhanced climatic warming in the Tibetan plateau due to doubling CO2: A model study. *Climate Dynamics*, *20*(4), 401–413. https://doi.org/10.1007/s00382-002-0282-4

Chen, X., Liu, Y., & Wu, G. (2017). Understanding the surface temperature cold bias in CMIP5 AGCMs over the Tibetan Plateau. *Advances in Atmospheric Sciences*, *34*(12), 1447–1460. https://doi.org/10.1007/s00376-017-6326-9

Chen, X., Long, D., Hong, Y., Liang, S., & Hou, A. (2017). Observed radiative cooling over the Tibetan Plateau for the past three decades driven by snow cover-induced surface albedo anomaly. *Journal of Geophysical Research: Atmospheres*, *122*(12), 6170–6185. https://doi.org/10.1002/2017JD026652

China Meteorological Administration/China. (2005). RADI_MUL_CHN_DAY_CES_STATION: The ground measurements of surface downward shortwave radiation, daily Data [Dataset]. Research Data Archive at China Meteorological Data Service Center. Retrieved from https://data.cma.cn/data/cdcdetail/dataCode/RADI_MUL_CHN_DAY.html

China Meteorological Administration/China. (2012). SURF_CLI_CHN_MUL_DAY V3.0: The observed daily ground surface temperature data, Version 3.0 [Dataset]. Research Data Archive at China Meteorological Data Service Center. Retrieved from http://101.200.76.197/data/dtail/dataCode/SURF_CLI_CHN_MUL_DAY_V3.0.html

China Meteorological Administration/China. (2021). CRA: The first-generation 40-yr global atmosphere and land reanalysis product, monthly data [Dataset]. Research Data Archive at the China Meteorological Data Service Center. https://doi.org/10.12065/2.C.GLB.2019.9.v1

Colman, R. A. (2013). Surface albedo feedbacks from climate variability and change. *Journal of Geophysical Research: Atmospheres*, *118*(7), 2827–2834. https://doi.org/10.1002/jgrd.50230

Dai, L., Che, T., & Ding, Y. (2015). Inter-calibrating SMMR, SSM/I and SSMI/S data to improve the consistency of snow-depth products in China. *Remote Sensing*, *7*(6), 7212–7230. https://doi.org/10.3390/rs70607212

Dee, D. P., Uppala, S. M., Simmons, A. J., Berrisford, P., Poli, P., Kobayashi, S., et al. (2011). The ERA-Interim reanalysis: Configuration and performance of the data assimilation system. *Quarterly Journal of the Royal Meteorological Society*, *137*(656), 553–597. https://doi.org/10.1002/qj.828

Duan, A., & Wu, G. (2006). Change of cloud amount and the climate warming on the Tibetan Plateau. *Geophysical Research Letters*, *33*(22), 1–5. https://doi.org/10.1029/2006GL027946

Duan, A., & Xiao, Z. (2015). Does the climate warming hiatus exist over the Tibetan Plateau? *Scientific Reports*, *5*, 1–9. https://doi.org/10.1038/srep13711

European Centre for Medium-Range Weather Forecasts/Europe. (2012). ERA interim: ERA interim monthly means of daily means [Dataset]. MediumRange. Retrieved from https://apps.ecmwf.int/datasets/data/interim-mdfa/levtype=sfc/

European Centre for Medium-Range Weather Forecasts/Europe. (2019). ERA5: ERA5-monthly averaged data on single levels from 1979 to present [Dataset]. Research Data Archive at the Climate Data Store. https://doi.org/10.24381/cds.f17050d7

Eyring, V., Bony, S., Meehl, G. A., Senior, C. A., Stevens, B., Stouffer, R. J., & Taylor, K. E. (2016). Overview of the coupled model Intercomparison Project Phase 6 (CMIP6) experimental design and organization. *Geoscientific Model Development*, *9*(5), 1937–1958. https://doi.org/10.5194/gmd-9-1937-2016

Feng, F., & Wang, K. (2019). Determining factors of monthly to decadal variability in surface solar radiation in China: Evidences from current reanalyses. *Journal of Geophysical Research: Atmospheres*, *124*(16), 9161–9182. https://doi.org/10.1029/2018JD030214

Flanner, M. G., Shell, K. M., Barlage, M., Perovich, D. K., & Tschudi, M. A. (2011). Radiative forcing and albedo feedback from the Northern Hemisphere cryosphere between 1979 and 2008. *Nature Geoscience*, *4*(3), 151–155. https://doi.org/10.1038/ngeo1062

Fujiwara, M., Wright, J. S., Manney, G. L., Gray, L. J., Anstey, J., Birner, T., et al. (2017). Introduction to the SPARC reanalysis Intercomparison Project (S-rip) and overview of the reanalysis systems. *Atmospheric Chemistry and Physics*, *17*(2), 1417–1452. https://doi.org/10.5194/acp-17-1417-2017

Gao, K., Duan, A., Chen, D., & Wu, G. (2019). Surface energy budget diagnosis reveals possible mechanism for the different warming rate among Earth's three poles in recent decades. *Science Bulletin*, *64*(16), 1140–1143. https://doi.org/10.1016/j.scib.2019.06.023

Gao, Y., Xu, J., & Chen, D. (2015). Evaluation of WRF mesoscale climate simulations over the Tibetan Plateau during 1979–2011. *Journal of Climate*, *28*(7), 2823–2841. https://doi.org/10.1175/JCLI-D-14-00300.1

Ghan, S. J., Liu, X., Easter, R. C., Zaveri, R., Rasch, P. J., Yoon, J. H., & Eaton, B. (2012). Toward a minimal representation of aerosols in climate models: Comparative decomposition of aerosol direct, semidirect, and indirect radiative forcing. *Journal of Climate*, *25*(19), 6461–6476. https://doi.org/10.1175/JCLI-D-11-00650.1

Global Modeling and Assimilation Office/America. (2008). MERRA 2D IAU diagnostic, time average 1-hourly V5.2.0 [Dataset]. Research Data Archive at the Goddard Earth Sciences Data and Information Services Center. Retrieved from https://disc.gsfc.nasa.gov/datasets/MAT1NXRAD_5.2.0/summary

Global Modeling and Assimilation Office/America. (2015). MERRA-2 2d, 1-hourly, time-averaged, single-level V5.12.4 [Dataset]. Research Data Archive at the Goddard Earth Sciences Data and Information Services Center. Retrieved from https://disc.gsfc.nasa.gov/datasets/M2T1NXRAD_5.12.4/summary

Guo, H., Wang, X., Wang, T., Ma, Y., Ryder, J., Zhang, T., et al. (2018). Spring snow-Albedo feedback analysis over the Third Pole: Results from satellite observation and CMIP5 model simulations. *Journal of Geophysical Research: Atmospheres*, *123*(2), 750–763. https://doi.org/10.1002/2017JD027846

He, T., Liang, S., & Song, D. (2014). Analysis of global land surface albedo climatology and spatial-temporal variation during 1981–2010 from multiple satellite products. *Journal of Geophysical Research: Atmospheres*, *119*, 10281–10298. https://doi.org/10.1002/2014JD021667

He, T., Liang, S., Yu, Y., Wang, D., Gao, F., & Liu, Q. (2013). Greenland surface albedo changes in July 1981-2012 from satellite observations. *Environmental Research Letters*, *8*(4). https://doi.org/10.1088/1748-9326/8/4/044043

He, Y., Wang, K., Zhou, C., & Wild, M. (2018). A revisit of global dimming and brightening based on the sunshine duration. *Geophysical Research Letters*, *45*(9), 4281–4289. https://doi.org/10.1029/2018GL077424

Hersbach, H., Bell, B., Berrisford, P., Biavati, G., Horányi, A., Muñoz Sabater, J., et al. (2019). *ERA5 monthly averaged data on single levels from 1979 to present*. Copernicus Climate Change Service (C3S) Climate Data Store (CDS). https://doi.org/10.24381/cds.f17050d7

Japan Meteorological Agency/Japan. (2013). JRA-55: Japanese 55-year reanalysis, daily 3-hourly and 6-hourly data [Dataset]. Research Data Archive at the National Center for Atmospheric Research, Computational and Information Systems Laboratory. https://doi.org/10.5065/D6HH6H41

Ji, P., Yuan, X., & Li, D. (2020). Atmospheric radiative processes accelerate ground surface warming over the southeastern Tibetan plateau during 1998–2013. *Journal of Climate*, *33*(5), 1881–1895. https://doi.org/10.1175/JCLI-D-19-0410.1

Ji, Z., Kang, S., Cong, Z., Zhang, Q., & Yao, T. (2015). Simulation of carbonaceous aerosols over the Third Pole and adjacent regions: Distribution, transportation, deposition, and climatic effects. *Climate Dynamics*, *45*(9–10), 2831–2846. https://doi.org/10.1007/s00382-015-2509-1

Jiang, Y., Chen, F., Gao, Y., Barlage, M., & Li, J. (2019). Using multisource satellite data to assess recent snow-cover variability and uncertainty in the Qinghai–Tibet Plateau. *Journal of Hydrometeorology*, *20*(7), 1293–1306. https://doi.org/10.1175/JHM-D-18-0220.1

Jiang, Y., Chen, F., Gao, Y., He, C., Barlage, M., & Huang, W. (2020). Assessment of uncertainty sources in snow cover simulation in the Tibetan plateau. *Journal of Geophysical Research: Atmospheres*, *125*(18), 1–17. https://doi.org/10.1029/2020JD032674

Kang, S., Zhang, Q., Qian, Y., Ji, Z., Li, C., Cong, Z., et al. (2019). Linking atmospheric pollution to cryospheric change in the Third Pole region: Current progress and future prospects. *National Science Review*, *6*(4), 796–809. https://doi.org/10.1093/nsr/nwz031

Karlsson, K. G., Anttila, K., Trentmann, J., Stengel, M., Fokke Meirink, J., Devasthale, A., et al. (2017). CLARA-A2: The second edition of the CM SAF cloud and radiation data record from 34 years of global AVHRR data. *Atmospheric Chemistry and Physics*, *17*(9), 5809–5828. https://doi.org/10.5194/acp-17-5809-2017

Karlsson, K. G., Anttila, K., Trentmann, J., Stengel, M., Fokke Meirink, J., Devasthale, A., et al. (2017). CLARA-A2: CM SAF cLoud, albedo and surface RAdiation dataset from AVHRR data—edition 2 [Dataset]. Satellite Application Facility on Climate Monitoring. https://doi.org/10.5676/EUM_SAF_CM/CLARA_AVHRR/V002

Kobayashi, S., Ota, Y., Harada, Y., Ebita, A., Moriya, M., Onoda, H., et al. (2015). The JRA-55 reanalysis: General specifications and basic characteristics. *Journal of the Meteorological Society of Japan*, *93*(1), 5–48. https://doi.org/10.2151/jmsj.2015-001

Kuang, X., & Jiao, J. J. (2015). Review on climate change on the Tibetan Plateau during the last half century. *Journal of Geophysical Research: Atmospheres*, *121*, 3979–4007. https://doi.org/10.1002/2015JD024728

Lei, Y., Letu, H., Shang, H., & Shi, J. (2020). Cloud cover over the Tibetan plateau and eastern China: A comparison of ERA5 and ERA-interim with satellite observations. *Climate Dynamics*, *54*(5–6), 2941–2957. https://doi.org/10.1007/s00382-020-05149-x

Li, W., Hu, S., Hsu1, P.-C., Guo, W., & Wei, J. (2020). Systematic bias of Tibetan Plateau snow cover in subseasonal-to-seasonal models. *The Cryosphere*, *14*, 3565–3579. https://doi.org/10.5194/tc-14-3565-2020

Li, Y., Wang, T., Zeng, Z. Z., Peng, S. S., Lian, X., & Piao, S. L. (2016). Evaluating biases in simulated land surface albedo from CMIP5 global climate models. *Journal of Geophysical Research: Atmospheres*, *121*, 6178–6190. https://doi.org/10.1002/2016JD024774

Liang, S., Zhao, X., Liu, S., Yuan, W., Cheng, X., Xiao, Z., et al. (2013). A long-term Global LAnd Surface Satellite (GLASS) data-set for environmental studies. *International Journal of Digital Earth*, *6*, 5–33. https://doi.org/10.1080/17538947.2013.805262

Liu, J., Schaaf, C., Strahler, A., Jiao, Z., Shuai, Y., Zhang, Q., et al. (2009). Validation of moderate resolution imaging spectroradiometer (MODIS) albedo retrieval algorithm: Dependence of Albedo on solar zenith angle. *Journal of Geophysical Research*, *114*(1), 1–11. https://doi.org/10.1029/2008JD009969

Liu, L., Ma, Y., Menenti, M., Su, R., Yao, N., & Ma, W. (2021). Improved parameterization of snow albedo in Noah coupled with weather research and forecasting: Applicability to snow estimates for the Tibetan plateau. *Hydrology and Earth System Sciences*, *25*(9), 4967–4981. https://doi.org/10.5194/hess-25-4967-2021

Liu, Q., Wang, L., Qu, Y., Liu, N., Liu, S., Tang, H., & Liang, S. (2013). Preliminary evaluation of the long-term GLASS albedo product. *International Journal of Digital Earth*, *6*, 69–95. https://doi.org/10.1080/17538947.2013.804601

Liu, X., & Chen, B. (2000). Climatic warming in the Tibetan Plateau during recent decades. *International Journal of Climatology*, *20*(14), 20001130. https://doi.org/10.1002/1097-0088

Loranty, M. M., Berner, L. T., Goetz, S. J., Jin, Y., & Randerson, J. T. (2014). Vegetation controls on northern high latitude snow-albedo feedback: Observations and CMIP5 model simulations. *Global Change Biology*, *20*(2), 594–606. https://doi.org/10.1111/gcb.12391

Lu, J., & Cai, M. (2009a). A new framework for isolating individual feedback processes in coupled general circulation climate models. Part I: Formulation. *Climate Dynamics*, *32*, 873–885. https://doi.org/10.1007/s00382-008-0425-3

Lu, J., & Cai, M. (2009b). Seasonality of polar surface warming amplification in climate simulations. *Geophysical Research Letters*, *36*(16), 1–6. https://doi.org/10.1029/2009GL040133

Ma, J., Zhang, T., Guan, X., Hu, X., Duan, A., & Liu, J. (2019). The dominant role of snow/ice Albedo feedback strengthened by black carbon in the enhanced warming over the Himalayas. *Journal of Climate*, *32*(18), 5883–5899. https://doi.org/10.1175/JCLI-D-18-0720.1

Manara, V., Beltrano, M. C., Brunetti, M., Maugeri, M., Sanchez-Lorenzo, A., Simolo, C., & Sorrenti, S. (2015). Sunshine duration variability and trends in Italy from homogenized instrumental time series (1936–2013). *Journal of Geophysical Research: Atmospheres*, *120*, 3622–3641. https://doi.org/10.1002/2014JD022560

Manninen, T., Riihelä, A., & de Leeuw, G. (2012). Atmospheric effect on the ground-based measurements of broadband surface albedo. *Atmospheric Measurement Techniques*, *5*(11), 2675–2688. https://doi.org/10.5194/amt-5-2675-2012

Orsolini, Y., Wegmann, M., Dutra, E., Liu, B., Balsamo, G., Yang, K., et al. (2019). Evaluation of snow depth and snow cover over the Tibetan Plateau in global reanalyses using in situ and satellite remote sensing observations. *The Cryosphere*, *13*(8), 2221–2239. https://doi.org/10.5194/tc-13-2221-2019

Pan, Z., Mao, F., Gong, W., Min, Q., & Wang, W. (2017). The warming of Tibetan Plateau enhanced by 3D variation of low-level clouds during daytime. *Remote Sensing of Environment*, *198*, 363–368. https://doi.org/10.1016/j.rse.2017.06.024

Pang, G., Chen, D., Wang, X., & Lai, H. W. (2022). Spatiotemporal variations of land surface albedo and associated influencing factors on the Tibetan Plateau. *Science of the Total Environment*, *804*, 150100. https://doi.org/10.1016/j.scitotenv.2021.150100

Qin, D., Liu, S., & Li, P. (2006). Snow cover distribution, variability, and response to climate change in Western China. *Journal of Climate*, *19*(9), 1820–1833. https://doi.org/10.1175/jcli3694.1

Qu, X., & Hall, A. (2014). On the persistent spread in snow-albedo feedback. *Climate Dynamics*, *42*(1–2), 69–81. https://doi.org/10.1007/s00382-013-1774-0

Qu, X., Huang, G., & Zhu, L. (2019). The CO2-induced sensible heat changes over the Tibetan Plateau from November to April. *Climate Dynamics*, *53*(9–10), 5623–5635. https://doi.org/10.1007/s00382-019-04887-x

Rangwala, I., & Miller, J. R. (2012). Climate change in mountains: A review of elevation-dependent warming and its possible causes. *Climatic Change*, *114*(3–4), 527–547. https://doi.org/10.1007/s10584-012-0419-3

Rangwala, I., Miller, J. R., & Xu, M. (2009). Warming in the Tibetan Plateau: Possible influences of the changes in surface water vapor. *Geophysical Research Letters*, *36*(6), 1–6. https://doi.org/10.1029/2009GL037245

Reichle, R. H., Draper, C. S., Liu, Q., Girotto, M., Mahanama, S. P. P., Koster, R. D., & De Lannoy, G. J. M. (2017). Assessment of MERRA-2 land surface hydrology estimates. *Journal of Climate*, *30*(8), 2937–2960. https://doi.org/10.1175/JCLI-D-16-0720.1

Rienecker, M. M., Suarez, M. J., Gelaro, R., Todling, R., Bacmeister, J., Liu, E., et al. (2011). MERRA: NASA's modern-era retrospective analysis for research and applications. *Journal of Climate*, *24*(14), 3624–3648. https://doi.org/10.1175/JCLI-D-11-00015.1

Shi, Q., & Liang, S. (2013a). Characterizing the surface radiation budget over the Tibetan plateau with ground-measured, reanalysis, and remote sensing data sets: 1. Methodology. *Journal of Geophysical Research: Atmospheres*, *118*, 9642–9657. https://doi.org/10.1002/jgrd.50720

Shi, Q., & Liang, S. (2013b). Characterizing the surface radiation budget over the Tibetan Plateau with ground-measured, reanalysis, and remote sensing data sets. Part 2: Spatiotemporal analysis. *Journal of Geophysical Research: Atmospheres*, *118*, 8921–8934. https://doi.org/10.1002/jgrd.50719

Su, F., Duan, X., Chen, D., Hao, Z., & Cuo, L. (2013). Evaluation of the global climate models in the CMIP5 over the Tibetan Plateau. *Journal of Climate*, *26*(10), 3187–3208. https://doi.org/10.1175/JCLI-D-12-00321.1

Su, J., Duan, A., & Xu, H. (2017). Quantitative analysis of surface warming amplification over the Tibetan Plateau after the late 1990s using surface energy balance equation. *Atmospheric Science Letters*, *18*(3), 112–117. https://doi.org/10.1002/asl.732

Tang, W. J., Yang, K., Qin, J., Cheng, C. C. K., & He, J. (2011). Solar radiation trend across China in recent decades: A revisit with quality controlled data. *Atmospheric Chemistry and Physics*, *11*(1), 393–406. https://doi.org/10.5194/acp-11-393-2011

Thackeray, C. W., Fletcher, C. G., & Derksen, C. (2019). Diagnosing the impacts of Northern Hemisphere surface albedo biases on simulated climate. *Journal of Climate*, *32*(6), 1777–1775. https://doi.org/10.1175/JCLI-D-18-0083.1

Wang, K., Ma, Q., Li, Z., & Wang, J. (2015). Decadal variability of surface incident solar radiation over China: Observations, satellite retrievals, and reanalyses. *Journal of Geophysical Research: Atmospheres*, *120*, 6500–6514. https://doi.org/10.1002/2015JD023420

Wang, K. C., Dickinson, R. E., Wild, M., & Liang, S. (2012). Atmospheric impacts on climatic variability of surface incident solar radiation. *Atmospheric Chemistry and Physics*, *12*(20), 9581–9592. https://doi.org/10.5194/acp-12-9581-2012

Wang, M., Yao, S., Jiang, L., Liu, Z., Shi, C., Hu, K., et al. (2018). Collection and pre-processing of satellite remote-sensing data in CRA-40 (CMA's global atmospheric ReAnalysis). *Advances in Meteorological Science and Technology*, *8*(1). https://doi.org/10.3969/j.issn.2095-1973.2018.01.021

Wang, W., Yang, K., Zhao, L., Zheng, Z., Lu, H., Mamtimin, A., et al. (2020). Characterizing surface albedo of shallow fresh snow and its importance for snow ablation on the interior of the Tibetan plateau. *Journal of Hydrometeorology*, *21*(4), 815–827. https://doi.org/10.1175/jhm-d-19-0193.1

Wang, Z., Wu, R., & Huang, G. (2018). Low-frequency snow changes over the Tibetan Plateau. *International Journal of Climatology*, *38*(2), 949–963. https://doi.org/10.1002/joc.5221

Wild, M. (2016). Decadal changes in radiative fluxes at land and ocean surfaces and their relevance for global warming. *Wiley Interdisciplinary Reviews: Climate Change*, *7*(1), 91–107. https://doi.org/10.1002/wcc.372

Wu, T., & Wu, G. (2004). An empirical formula to compute snow cover fraction in GCMs. *Advances in Atmospheric Sciences*, *21*(4), 529–535. https://doi.org/10.1007/BF02915720

Wu, Y., Yang, S., Hu, X., & Wei, W. (2020). Process-based attribution of long-term surface warming over the Tibetan Plateau. *International Journal of Climatology*(15), 6410–6422. https://doi.org/10.1002/joc.6589

Yan, Y., You, Q., Wu, F., Pepin, N., & Kang, S. (2020). Surface mean temperature from the observational stations and multiple reanalyses over the Tibetan Plateau. *Climate Dynamics*, *55*(9–10), 2405–2419. https://doi.org/10.1007/s00382-020-05386-0

Yang, K., Ding, B., Qin, J., Tang, W., Lu, N., & Lin, C. (2012). Can aerosol loading explain the solar dimming over the Tibetan Plateau? *Geophysical Research Letters*, *39*(20), 1–5. https://doi.org/10.1029/2012GL053733

Yang, K., Pinker, R. T., Ma, Y., Koike, T., Wonsick, M. M., Cox, S. J., et al. (2008). Evaluation of satellite estimates of downward shortwave radiation over the Tibetan Plateau. *Journal of Geophysical Research*, *113*(17). https://doi.org/10.1029/2007JD009736

You, Q., Cai, Z., Pepin, N., Chen, D., Ahrens, B., Jiang, Z., et al. (2021). Warming amplification over the Arctic Pole and Third Pole: Trends, mechanisms and consequences. *Earth-Science Reviews*, *217*, 103625. https://doi.org/10.1016/j.earscirev.2021.103625

You, Q., Jiao, Y., Lin, H., Min, J., Kang, S., Ren, G., & Meng, X. (2014). Comparison of NCEP/NCAR and ERA-40 total cloud cover with surface observations over the Tibetan Plateau. *International Journal of Climatology*, *34*(8), 2529–2537. https://doi.org/10.1002/joc.3852

You, Q., Sanchez-Lorenzo, A., Wild, M., Folini, D., Fraedrich, K., Ren, G., & Kang, S. (2013). Decadal variation of surface solar radiation in the Tibetan Plateau from observations, reanalysis and model simulations. *Climate Dynamics*, *40*(7–8), 2073–2086. https://doi.org/10.1007/s00382-012-1383-3

Zhang, J., Wu, T., Shi, X., Zhang, F., Li, J., Chu, M., et al. (2019). BCC BCC-ESM1 model output prepared for CMIP6 CMIP amip. Version 20190202 [Dataset]. Earth System Grid Federation. https://doi.org/10.22033/ESGF/CMIP6.2851

Zhang, R., Wang, H., Fu, Q., Rasch, P. J., & Wang, X. (2019). Unraveling driving forces explaining significant reduction in satellite-inferred Arctic surface albedo since the 1980s. *Proceedings of the National Academy of Sciences of the United States of America*, *116*(48), 23947–23953. https://doi.org/10.1073/pnas.1915258116

Zhang, X., Lu, N., Jiang, H., & Yao, L. (2020). Evaluation of reanalysis surface incident solar radiation data in China. *Scientific Reports*, *10*(1), 1–20. https://doi.org/10.1038/s41598-020-60460-1

Zhu, F., Cuo, L., Zhang, Y., Luo, J. J., Lettenmaier, D. P., Lin, Y., & Liu, Z. (2018). Spatiotemporal variations of annual shallow soil temperature on the Tibetan Plateau during 1983–2013. *Climate Dyn*, *51*, 2209–2227. https://doi.org/10.1007/s00382-017-4008-z

References From the Supporting Information

Bethke, I., Wang, Y., Counillon, F., Kimmritz, M., Fransner, F., Samuelsen, A., et al. (2019). NCC NorCPM1 model output prepared for CMIP6 CMIP amip. Version 20191031 [Dataset]. Earth System Grid Federation. https://doi.org/10.22033/ESGF/CMIP6.10863

Boucher, O., Denvil, S., Levavasseur, G., Cozic, A., Caubel, A., Foujols, M.-A., et al. (2018). IPSL IPSL-CM6A-LR model output prepared for CMIP6 CMIP amip. Version 20191003 [Dataset]. Earth System Grid Federation. https://doi.org/10.22033/ESGF/CMIP6.5113

Byun, Y.-H., Lim, Y.-J., Sung, H. M., Kim, J., Sun, M., & Kim, B.-H. (2019). NIMS-KMA KACE1.0-G model output prepared for CMIP6 CMIP amip. Version 20190813 [Dataset]. Earth System Grid Federation. https://doi.org/10.22033/ESGF/CMIP6.8350

Cao, J., & Wang, B. (2019). NUIST NESMv3 model output prepared for CMIP6 CMIP amip. Version 20190812 [Dataset]. Earth System Grid Federation. https://doi.org/10.22033/ESGF/CMIP6.8720

Danabasoglu, G. (2019). NCAR CESM2 model output prepared for CMIP6 CFMIP piSST. Version 20190218 [Dataset]. Earth System Grid Federation. https://doi.org/10.22033/ESGF/CMIP6.7736

Danabasoglu, G. (2019). NCAR CESM2-WACCM model output prepared for CMIP6 CMIP amip. Version 20190220 [Dataset]. Earth System Grid Federation. https://doi.org/10.22033/ESGF/CMIP6.10041

Danabasoglu, G. (2020a). NCAR CESM2-FV2 model output prepared for CMIP6 CMIP amip. Version 20200305 [Dataset]. Earth System Grid Federation. https://doi.org/10.22033/ESGF/CMIP6.11287

Danabasoglu, G. (2020b). NCAR CESM2-WACCM-FV2 model output prepared for CMIP6 CMIP amip. Version 20200305 [Dataset]. Earth System Grid Federation. https://doi.org/10.22033/ESGF/CMIP6.11288

Dix, M., Bi, D., Dobrohotoff, P., Fiedler, R., Harman, I., Law, R., et al. (2019). CSIRO-ARCCSS ACCESS-CM2 model output prepared for CMIP6 CMIP amip. Version 20191108 [Dataset]. Earth System Grid Federation. https://doi.org/10.22033/ESGF/CMIP6.4239

EC-Earth Consortium (EC-Earth). (2020). EC-Earth-Consortium EC-Earth3-AerChem model output prepared for CMIP6 CMIP amip. Version 20200910 [Dataset]. Earth System Grid Federation. https://doi.org/10.22033/ESGF/CMIP6.4530

EC-Earth Consortium (EC-Earth). (2021). EC-Earth-Consortium EC-Earth-3-CC model output prepared for CMIP6 CMIP amip. Version 20210209zz[Dataset]. Earth System Grid Federation. https://doi.org/10.22033/ESGF/CMIP6.4531

Huang, W. (2020). THU CIESM model output prepared for CMIP6 CMIP amip. Version 20200417 [Dataset]. Earth System Grid Federation. https://doi.org/10.22033/ESGF/CMIP6.8810

Jungclaus, J., Bittner, M., Wieners, K.-H., Wachsmann, F., Schupfner, M., Legutke, S., et al. (2019). MPI-M MPI-ESM1.2-HR model output prepared for CMIP6 CMIP amip. Version 20190710 [Dataset]. Earth System Grid Federation. https://doi.org/10.22033/ESGF/CMIP6.6463

Li, L. (2019). CAS FGOALS-g3 model output prepared for CMIP6 CMIP amip. Version 20191108 [Dataset]. Earth System Grid Federation. https://doi.org/10.22033/ESGF/CMIP6.3183

Lovato, T., & Peano, D. (2020). CMCC CMCC-CM2-SR5 model output prepared for CMIP6 CMIP amip. Version 20200717 [Dataset]. Earth System Grid Federation. https://doi.org/10.22033/ESGF/CMIP6.3737

Neubauer, D., Ferrachat, S., Siegenthaler-Le D, C., Stoll, J., Folini, D. S., Tegen, I., et al. (2019). HAMMOZ-Consortium MPI-ESM1.2-HAM model output prepared for CMIP6 CMIP amip. Version 20190628 [Dataset]. Earth System Grid Federation. https://doi.org/10.22033/ESGF/CMIP6.5001

Park, S., & Shin, J. (2019). SNU SAM0-UNICON model output prepared for CMIP6 CMIP amip. Version 20190323 [Dataset]. Earth System Grid Federation. https://doi.org/10.22033/ESGF/CMIP6.7784

Raghavan, K., Panickal, S., Narayanasetti, S., Gopinathan, P. A., Choudhury, A. D., & Singh, M. (2020). CCCR-IITM IITM-ESM model output prepared for CMIP6 CMIP amip. Version 20200915 [Dataset]. Earth System Grid Federation. https://doi.org/10.22033/ESGF/CMIP6.3517

Scoccimarro, E., Bellucci, A., & Peano, D. (2021). CMCC CMCC-CM2-HR4 model output prepared for CMIP6 CMIP amip. Version 20210309 [Dataset]. Earth System Grid Federation. https://doi.org/10.22033/ESGF/CMIP6.3735

Swart, N. C., Cole, J. N. S., Kharin, V. V., Lazare, M., Scinocca, J. F., Gillett, N. P., et al. (2019). CCCma CanESM5 model output prepared for CMIP6 CMIP amip. Version 20190429 [Dataset]. Earth System Grid Federation. https://doi.org/10.22033/ESGF/CMIP6.3535

Tatebe, H., & Watanabe, M. (2018). MIROC MIROC6 model output prepared for CMIP6 CMIP amip. Version 20181214 [Dataset]. Earth System Grid Federation. https://doi.org/10.22033/ESGF/CMIP6.5422

Volodin, E., Mortikov, E., Gritsun, A., Lykossov, V., Galin, V., Diansky, N., et al. (2019). INM INM-CM4-8 model output prepared for CMIP6 CMIP amip. Version 20190528 [Dataset]. Earth System Grid Federation. https://doi.org/10.22033/ESGF/CMIP6.4934

Volodin, E., Mortikov, E., Gritsun, A., Lykossov, V., Galin, V., Diansky, N., et al. (2019). INM INM-CM5-0 model output prepared for CMIP6 CMIP amip. Version 20190610 [Dataset]. Earth System Grid Federation. https://doi.org/10.22033/ESGF/CMIP6.4935

Wieners, K.-H., Giorgetta, M., Jungclaus, J., Reick, C., Esch, M., Bittner, M., et al. (2019). MPI-M MPI-ESM1.2-LR model output prepared for CMIP6 CMIP amip. Version 20190815 [Dataset]. Earth System Grid Federation. https://doi.org/10.22033/ESGF/CMIP6.6464

Yu, Y. (2018). CAS FGOALS-f3-L model output prepared for CMIP6 CMIP amip. Version 20190422 [Dataset]. Earth System Grid Federation. https://doi.org/10.22033/ESGF/CMIP6.3182

Yukimoto, S., Koshiro, T., Kawai, H., Oshima, N., Yoshida, K., Urakawa, S., et al. (2019). MRI MRI-ESM2.0 model output prepared for CMIP6 CMIP amip. Version 20190308 [Dataset]. Earth System Grid Federation. https://doi.org/10.22033/ESGF/CMIP6.6758

Ziehn, T., Chamberlain, M., Lenton, A., Law, R., Bodman, R., Dix, M., et al. (2019). CSIRO ACCESS-ESM1.5 model output prepared for CMIP6 CMIP amip. Version 20191114 [Dataset]. Earth System Grid Federation. https://doi.org/10.22033/ESGF/CMIP6.4240